Eidgenössische Technische Hochschule Zürich
Swiss Federal Institute of Technology Zurich

Quantum Collapse Models

Semester Thesis

Leo Konzett
lkonzett@ethz.ch

Laboratory for Solid State Physics
Departement of Physics, D-PHYS
ETH Zürich

Supervisors:
Prof. Dr. Yiwen Chu
Dr. Matteo Fadel

April 4, 2023

Abstract

Quantum mechanics has passed all precision tests with flying colours, but it still seems to be in conflict with common sense. Why are objects around us never found in superpositions of states that would be impossible in a classical description? One may emphasize the smallness of Planck's constant, or point to decoherence theory, which describes how a system will effectively lose its quantum features when coupled to a quantum environment of sufficient size. More radically, *objective collapse* theories ascertain that quantum mechanics breaks down beyond a certain mass or complexity scale, and that standard quantum mechanics is but an approximation to a more general theory. These theories posit that quantum theory must be modified at a fundamental level, designed to induce an objective collapse of the wave function above a critical mass scale of a given quantum system, thereby restoring classicality. The dynamics induced by collapse models are controlled by a few parameters and give predictions that differ from standard quantum mechanics. Most importantly, these differences can be verified experimentally, and thus enable to place strong bounds on the values of these parameters. In this report, we calculate upper bounds for two collapse parameters obtained from two different experimental setups. We will show that the bounds placed by the experimental data are weaker than those coming from non-interferometric tests of collapse models.

Contents

Chapter 1

Introduction

1.1. Motivation

The classical dynamics of a system of particles having a Hamiltonian H is described in phase space (q_n, p_n) by Hamilton's equation of motion

$$\frac{d}{dt}q_n = \frac{\partial H}{\partial p_n},\ \frac{d}{dt}p_n = -\frac{\partial H}{\partial q_n} \tag{1.1}$$

The state of the system at an initial time t_0 is a point in the phase space, and the equations of motion determine the location of the system point at a later time. An equivalent description of the dynamics is through the Hamilton-Jacobi equation

$$-\frac{\partial S}{\partial t} = H\left(q_n, \frac{\partial S}{\partial q_n}\right) \tag{1.2}$$

where S is the *action* of the system. In contrast, quantum dynamics is described by the time evolution a system's wavefunction Ψ, which is a normalized element of a Hilbert space and obeys the Schroedinger equation. For a single particle n of mass m moving in one dimension, the Schroedinger equation, after defining $\psi = e^{iS/\hbar}$, is

$$-\frac{\partial S}{\partial t} = \frac{1}{2m}\left(\frac{\partial S}{\partial t}\right)^2 + V(q_n) - \frac{i\hbar}{2m}\frac{\partial^2 S}{\partial^2 q_n} \tag{1.3}$$

In the approximation in which the last term in this equation can be neglected, this equation reduces to the classical Hamilton-Jacobi equation. This essentially corresponds to the limit $S \gg \hbar$. There is thus a well-defined sense in which the Schroedinger (quantum) equation goes over the the Hamilton-Jacobi (classical) equation, and a description of the dynamics in Hilbert space (quantum) gets replaced by a description in terms of evolution of position and momentum coordinates (classical) in phase space. Yet, there is an aspect which gets lost in the limiting process: The Schroedinger equation is *linear*, whereas the Hamilton-Jacobi equation is *non-linear*: If S_1 is a solution corresponding to one trajectory in phase space, and S_2 is a solution corresponding to another such trajectory, then clearly $a_1 S_1 + a_2 s_2$ is not a solution of this equation. In particular, if Ψ_1 is a wave-packet which is peaked around one classical solution and Ψ_2 is a wave-packet peaked around another classical solution, quantum mechanics predicts that the sum of these two wave-packets is also a solution, and in principle such solutions should be observed in nature.

Figure 1.1.: Cartoon comparison of microscopic and macroscopic systems: While the microscopic particle can be in a superposition state, the macroscopic pointer system is always localized.

However, according to classical mechanics, such a superposition is not a solution of the equations of motion, nor is it observed in the macroscopic world around us. Naively, we believe that classical mechanics, which applies to macroscopic systems, is a limiting case of quantum mechanics, and hence quantum mechanics should apply to large systems as well. Why is it then that macroscopic objects which obey the rules of classical mechanics are not found in superposition of different position states, in spite of quantum theory suggesting otherwise? There is no unique universally accepted answer to this question.

1.2. The measurement problem

The absence of macroscopic superpositions is closely related to the *measurement* problem in quantum theory, which we will briefly summarize in the following. For a detailed treatment in the context of collapse models, see chapter III of [1]. Let us consider a macroscopic apparatus with which we measure the spin of a single particle. The corresponding Hilbert space is two-dimensional Hilbert, with basis kets $\{|\uparrow\rangle, |\downarrow\rangle\}$. The apparatus measures the spin via a pointer that can take two positions: "Left" (if $|\uparrow\rangle$ is measured) and "Right" (if $|\downarrow\rangle$ is measured). As such, the Hilbert space for the pointer has basis kets $\{|\leftarrow\rangle, |\rightarrow\rangle\}$. Let us assume that the particle is in a superposition state, e.g. $|\Psi\rangle = c_\uparrow |\uparrow\rangle + c_\downarrow |\downarrow\rangle$, where the complex coefficients are probability amplitudes chosen such that their modulus squared sums to unity. By measuring the spin with the apparatus, the pointer state cannot be described independently from the spin state. The resulting *entangled* state is a tensor product of the particle and pointer states and is given by

$$|\Psi\rangle = c_\uparrow |\uparrow\rangle \otimes |\leftarrow\rangle + c_\downarrow |\downarrow\rangle \otimes |\rightarrow\rangle \tag{1.4}$$

This state evolves continuously according to the Schrodinger equation, hence preserving the superposition. However, in an actual measurement, we never observe the pointer to point simultaneously to the left or to the right, as illustrated in Figure (1.1) Above a critical mass or complexity scale, the superposition principle seems to break down, and the pointer *collapses* to one of its basis states, as illustrated in Figure (1.2). This collapse is certainly not continuous and breaks the superposition that should be preserved according the the Schrodinger equation. Even worse, the measurement outcome

Figure 1.2.: Cartoon of reduction process: Entangling a microscopic degree of freedom (spin) with a macrosopic one (pointer) leads to a reduction in the state vector. The collapse to the state $|\uparrow\rangle \otimes |\leftarrow\rangle$ happens with probability $|c_\uparrow|^2$.

is probabilistic, even though the Schrodinger equation predicts a deterministic evolution for the quantum state. As such, quantum theory seems two rely on two different evolution processes: There is the U (unitary) process, where the state changes smoothly, and the R (reduction) process, in which the state of the system changes instantaneously and randomly. As such, as soon as the particle becomes entangled with the macroscopic pointer, the superposition state collapses, and the spin state is either up or down:

$$|\Psi\rangle = c_\uparrow |\uparrow\rangle \otimes |\leftarrow\rangle + c_\downarrow |\downarrow\rangle \otimes |\rightarrow\rangle \xrightarrow{\text{Reduction R}} |\uparrow\rangle \otimes |\leftarrow\rangle \text{ or } |\downarrow\rangle \otimes |\rightarrow\rangle \tag{1.5}$$

The U process is supposed to control a system's dynamics all the time that the system is left alone, while the R process is called upon whenever we entangle a microscopic degree of freedom with a macroscopic one. The problem is then that no one has been able to characterize in general when a physical process should be considered macroscopic. How much mass, or degrees of freedom should an object have to be classified as macroscopic? In other words, where is the quantum-classical divide?

1.3. Interpretations of the Measurement problem

In the following, we present the most prominent interpretations of quantum mechanics dealing with the measurement problem, with a complete overview given in [2].

1.3.1. Copenhagen and Many-World interpretations

In Hugh Everett's many-worlds interpretation, there is only one wave function, the superposition of the entire universe. The act of measurement entangles different entities, e.g. an observer, a measuring instrument, and an electron/positron. The measurement hence induces correlations, and there is no R process or collapse postulate. In contrast, viewpoints that broadly fall within the *Copenhagen* interpretation accept the collapse postulate. In particular, they emphasize that the results provided by a measuring apparatus are essentially classical. As such, the device used to observe a system must be described in classical language, while the system under observation is treated in quantum terms. This is a particularly subtle issue for which Bohr and Heisenberg came to differing conclusions. According to Heisenberg, the boundary between classical and quantum can be shifted in either direction at the observer's discretion. That is, the observer has the freedom to move what the quantum to classical" cut without changing any physically meaningful predictions. On the other hand, Bohr argued both systems are quantum in

principle, and the object-instrument distinction (the "cut") is dictated by the experimental arrangement. For Bohr, the "cut" was not a change in the dynamical laws that govern the systems in question, but a change in the language applied to them.

1.3.2. Decoherence

In the 1980's, *decoherence* theories gained traction among the physics community. This viewpoint maintains that state vector reduction (the R process) can be understood as coming about because the environmental system under consideration becomes inextricably entangled with its environment. The environment is assumed to be extremely complicated and essentially 'random'. However, upon measurement, the observer only gains information about the system under consideration (e.g. the spin of a particle), and not about the environment, as illustrated in Figure (1.3). Most importantly, decoherence does not claim to provide a mechanism for the actual wave-function collapse; rather it puts forth a reasonable framework for the *appearance* of wave-function collapse. Decoherence is needed to understand why a quantum system begins to obey classical probability rules after interacting with its environment.

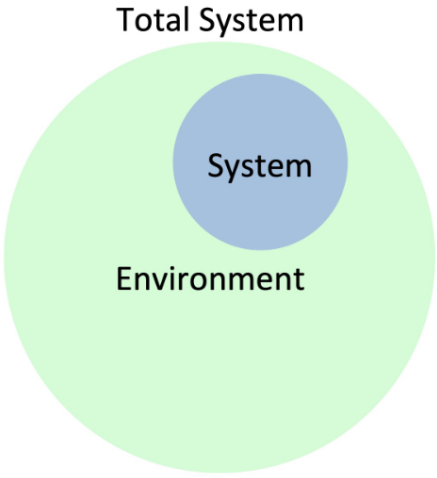

Figure 1.3.: A total, closed system divided into the system of interest, "System", and the environment. The interaction of the system of interest with the environment cannot be avoided (they become entangled), and we require an approach in which the environment can be effectively removed from the equations of motion. Mathematically, tracing out the environment degrees of freedom introduces a classical statistical uncertainty for the quantum state of the system.

1.3.3. Collapse models

An alternative interpretation is provided by collapse theories. There, the U and R processes are unified and described by a single equation that governs both processes. There is no observer and no measurement apparatus, and collapse arises simply because one designs the evolution equation to include it. Combining the U and R process means that the Schroedinger equation itself must be modified. This modification adds randomness to the previously deterministic equation. In general, all modifications to the Schroedinger equation must respect the principles outlined below:

1. Standard quantum theory is empirically verified for microscopic systems. The collapse process must be negligible for these systems.

2. To explain the absence of macroscopic superpositions, the collapse must be amplified for larger system. To avoid an arbitrary cut-off (the original criticism to Copenhagen interpretation), we need some kind of amplification mechanicsm.

3. The collapse process must account predicts *random* outcomes of measurements. In particular, they need to respect the Born rule.

4. To not violate the theory of relativity, collapse models must not allow for superluminal signalling.

These requirements are very demanding, and it is not clear from the outset why there should be a solution at all. In the following, we give a chronological overview over attempts to meet the above requirements, while at the same time emphasizing the most important ideas of collapse processes.

Chapter 2

Theory

The GRW is the first spontaneous collapse theory that was devised, being proposed by Ghirardi, Rimini & Weber in 1982 [3]. In the following years the field developed and different models were formulated, among which the CSL model [4], which is formulated in terms of identical particles; and the Diósi–Penrose model [5], which relates the spontaneous collapse to gravity. These models will be presented in the following.

2.1. GRW model

In GRW theory, the wave function (or state vector) represents the most accurate possible specification of the state of a physical system. As such, it differs from hidden-variable theories, according to which the wave function does not give a complete description of a physical system. The GRW models differs from standard quantum mechanics for the dynamical principles according to which the wave function evolves, and operates according to the following principles [3]:

1. Each particle of a system of n distinguishable particles, described by the multi-particle state vector $|\Psi\rangle$, undergoes a spontaneous localization process:

$$|\Psi\rangle \xrightarrow{\text{Localization}} \frac{\left|\Psi_x^i\right\rangle}{\sqrt{\langle\Psi_x^i|\Psi_x^i\rangle}} \tag{2.1}$$

   where $\left|\Psi_x^i\right\rangle = \hat{L}_x^i |\Psi\rangle$ is the state after the operator $\hat{L}_x^i$ has localized the i-th particle around the position x.

2. The localization process is random both in space and time. The jumps are Poisson distributed in time, with mean rate λ_{GRW}; the probability density for a jump to occur at position x is given by $P_i(x) = \left\langle\Psi_x^i\middle|\Psi_x^i\right\rangle$.

3. In the time interval between two localizations, the state vector evolves according to the Schroedinger equation.

4. The localization operator has a Gaussian form:

$$\hat{L}_x^i = \left(\frac{1}{\pi r_c^2}\right)^{\frac{3}{4}} e^{\frac{-(\hat{q}_i - x)^2}{2r_c^2}} \tag{2.2}$$

where $\hat{q}_i$ is the position operator of the i-th particle, and the r_c is the localization distance which will be described in more detail in Section (2.1.2).

2.1.1. Single particle in 1D

To see how the Gaussian operator $\hat{L}_x^i$ localizes the particle i at position x, consider a superposition of two Gaussian wave functions with spread σ, centered at $x = a$ and $x = -a$ respectively:

$$\psi(x) = \frac{1}{(\pi\sigma)^{1/4}} \left[e^{-\frac{(x-a)^2}{2\sigma^2}} + e^{-\frac{(x+a)^2}{2\sigma^2}} \right] \tag{2.3}$$

We assume that the particle undergoes a localization process at position $x = a$, i.e. we have

$$\psi_a(x) = \hat{L}_{x=a}\psi(x) = \mathcal{N} e^{-\frac{(x-a)^2}{2r_c^2}} \left[e^{-\frac{(x-a)^2}{2\sigma^2}} + e^{-\frac{(x+a)^2}{2\sigma^2}} \right] \tag{2.4}$$

where $\mathcal{N}$ is a normalization factor. We now make two assumptions: Firstly, each Gaussian is localized, i.e. $\sigma \ll r_c$. Secondly, the distance between the two Gaussian wave functions is larger than the localization length, i.e. $(2a \gg r_c)$. We then find [1]

$$\psi_a(x) \approx \mathcal{N}' \left[e^{-\frac{(x+a)^2}{2\sigma^2} - \frac{2a^2}{r_c^2}} + e^{-\frac{-(x-a)^2}{2\sigma^2}} \right] \tag{2.5}$$

We notice that the Gaussian that is hit by the localization operator is left unchanged (it was already localized), whereas the other one is exponentially suppressed. The particle thus becomes localized at $x = a$.

2.1.2. The collapse mechanism - choice of parameters

The collapse parameters λ_{GRW} and r_c are phenomenological constants, whose values are not fixed by any principle and should be understood as "new" constants of Nature, if collapse theory is indeed a correct description of Nature. λ_{GRW} sets the *mean* rate of collapse for a single particle, and thus determines how fast a superposition state reduces to one of its basis states. As such, it should be chosen such that microscopic objects are almost never localized, thus effectively recovering standard quantum mechanics. On the other hand, macroscopic systems should be localized within a very small fraction of a second. Ghirardi, Rimini & Weber originally set the value of the collapse rate to $\lambda_{\text{GRW}} = 10^{-16}\ s^{-1}$, meaning that a state reduction (collapse) process happens every 100 - 1000 million years for a single particle.

The localization length r_c specifies which kind of superpositions are effectively suppressed, as illustrated in Figure (2.1). It thus specifies a threshold between microscopic and macroscopic systems. The localization distance should be large with respect to atomic dimensions. In this way, even when one of the extremely infrequent localization processes takes place for a particle of an atomic system, the localization does not modify the internal structure of that system [1]. On the other hand, r_c must be chosen large

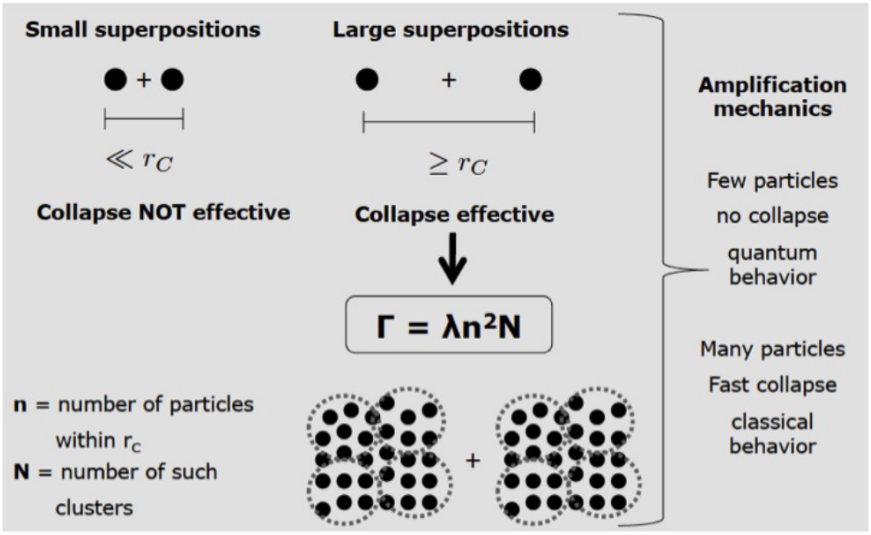

Figure 2.1.: Cartoon detailing the role of the localization length in reduction processes. Taken from [6].

enough to avoid the occurrence of spatial superpositions of a macroscopic object such as the measurement apparatus. There is broad consensus to set r_c within the mesoscopic scale, at $r_c = 10^{-7}m$.

2.1.3. Modification for ensembles

We can express the above principles more compactly using the density operator formalism. The localization process is Poissonian, and hence in a time interval dt there is a probability $\lambda_{\text{GRW}}dt$ that a collapse occurs. As such, the pure state $\rho = |\Psi\rangle\langle\Psi|$ gets transformed into the statistical mixture

$$|\Psi\rangle\langle\Psi| \to \int_V dx \hat{L}_x^i |\Psi\rangle\langle\Psi| \hat{L}_x^i = \hat{T}_i[\rho] \tag{2.6}$$

where $\hat{T}_i$ is a completely positive, trace-preserving map that acts on the i-th particle. Note that with probability $(1 - \lambda_{\text{GRW}})dt$, no collapse occurs, and $\hat{\rho}$ evolves according to the standard Schroedinger equation. We thus arrive at the following GRW master equation for N particles:

$$\frac{d}{dt}\rho(t) = -\frac{i}{\hbar}[\hat{H}, \rho(t)] - \sum_{i=1}^{N} \lambda_{\text{GRW}} \left(\rho(t) - \hat{T}_i[\rho(t)]\right) \tag{2.7}$$

where $\hat{H}$ is the Hamiltonian of the system, and the square brackets denote the commutator.

2.1.4. Amplification mechanism

We next consider a macroscopic system, e.g. the measurement apparatus, that consists of N particles. We describe the position of the particles in terms of center of mass (CM) and relative (R) position operators, i.e. $\hat{q}_i = \hat{Q}_{CM} + \hat{r}_i$. *If* the system Hamiltonian can be split into a center of mass Hamiltonian $\hat{H}_{\mathrm{CM}}$ and a relative Hamiltonian $\hat{H}_r$, the center of mass statistical operator ρ_{CM} can be shown to have the following master equation [1]:

$$\frac{d}{dt}\rho_{\mathrm{CM}}(t) = -\frac{i}{\hbar}[\hat{H}_{\mathrm{CM}}, \rho_{\mathrm{CM}}(t)] - \sum_{i=1}^{N} \lambda_{\mathrm{GRW}} \left(\rho_{\mathrm{CM}}(t) - \hat{T}_{\mathrm{CM}}[\rho_{\mathrm{CM}}(t)]\right) \tag{2.8}$$

where $\hat{T}_{\mathrm{CM}}$ is again a completely positive, trace-preserving map. We thus have an amplification mechanism: For a single particle in a spatial superposition state, a reduction process happens infrequently and the particle evolves according to the Schroedinger equation. For the measurement apparatus, the center of mass collapses with an amplified rate $\epsilon = N\lambda$. Using the GRW value for λ, and assuming that the apparatus consists of an Avogadro number of nucleons, we find a collapse rate $\epsilon = 10^7\ s^{-1}$.

2.1.5. Energy conservation

The GRW model gives a master equation for the density operator different from standard quantum dynamics (SQD). As such, the expectation values $\mathrm{Tr}(\hat{\rho}\hat{A})$ of an observable $\hat{A}$, or its variance, might differ from SQD predictions. Bassi & Ghirardi [1] showed that for a nucleon with mass m, the expectation value for the momentum operator $\hat{p}$ is identical to SQD: $\langle\hat{p}\rangle_{\mathrm{GRW}} = \langle\hat{p}\rangle_{\mathrm{SQD}}$. However, the momentum spread changes within a time t to [1]

$$(\hat{p} - \langle\hat{p}\rangle)^2_{\mathrm{GRW}} = (\hat{p} - \langle\hat{p}\rangle)^2_{\mathrm{SQD}} + \frac{\lambda_{\mathrm{GRW}}\hbar^2}{6m^2r_c^2}t^3 \tag{2.9}$$

We thus see that there is a diffusion rate induced by the collapse process. This introduces a steady amount of energy in the system

$$\langle E\rangle_{\mathrm{GRW}} = \langle E\rangle_{\mathrm{SQD}} + \frac{\lambda_{\mathrm{GRW}}\hbar^2}{4m}t \tag{2.10}$$

leading to a violation of the energy conservation principle. Although such an energy increase is negligible, this feature of the model is not appealing. For this reason, a *dissipative* extension of the GRW theory has been investigated [7]. Other drawbacks of the GRW theory include that it is a non-relativistic theory, and that it only applies to distinguishable particles.

2.2. The CSL model

The continuous spontaneous localization (CSL) model solves two aspects of the GRW model. First, it gives a continuous equation for the state vector in contrast to discrete

hitting processes. Second, it is applicable to identical particles. In the following, we present the CSL model in its standard form. Various extensions to the CSL model have been proposed, which include the *colored* CSL model, and the *dissipative* CSL model, which aims to preserve energy conservation [7].

A "continuous" hitting process requires a continuous interaction of the system under consideration with an external field that triggers the reduction. This external field is commonly called the *noise* field, and its existence is a postulate of the theory. The continuous reduction of the state vector to one of its eigenstates (as opposed to the sudden localization in GRW) is called *dynamical* reduction. The benefit of a continuous interaction is the possibility to write down a single equation (that governs the earlier U and R processes) at the level of the wave function, something that is not possible with the GRW model. In the GRW model, we only have a continuous equation for the density operator, but not for the state vector itself. In continuous collapse models, one obtains the updated equation that describes the evolution of the state vector in time by adding non-linear and stochastic terms to the standard Schrodinger equation. The two most popular models of this class are the QMUPL (Quantum Mechanics with Universal Position Localization) model and the CSL model. One of the essential differences between the two is the simpler mathematical structure of the QMUPL model: There, the noise field "lives" only in the time dimension, whereas the CSL noise field is spread both in time and space. A full derivation of the CSL modified Schrodinger equation is beyond the scope of this report, and can be found in [4]. Instead, we present important conceptual ideas of the dynamical reduction program.

2.2.1. Example

As an example, we consider a spin system with state vector $|\Psi_0\rangle$ at time $t = 0$, where we expand the state in the basis $\{|\uparrow\rangle, |\downarrow\rangle\}$:

$$|\Psi_0\rangle = |\uparrow\rangle\langle\uparrow| \, |\Psi_0\rangle + |\downarrow\rangle\langle\downarrow| \, |\Psi_0\rangle \tag{2.11}$$

In SQD, $x_\uparrow(0) = |\langle\uparrow|\Psi_0\rangle|^2$ and $x_\downarrow(0) = |\langle\downarrow|\Psi_0\rangle|^2$ are the probability amplitudes to find the system in spin state up or down, respectively, at time $t = 0$. For an isolated system, they stay constant for all times t, i.e. $x_\uparrow(0) = x_\uparrow(t)$. Contrary to that, the amplitudes aren't constant in collapse theory, as the system continuously interacts with the external noise field that triggers the collapse. We postulate that a reduction happens as soon as one of the now fluctuating amplitudes is equal to one and denote the collapse time by τ, i.e. a reduction happens if $x_{\uparrow,\mathrm{CSL}}(\tau) = 1$. The remaining amplitudes are equal to zero at the collapse time τ. We hence have

$$|\Psi_0\rangle_{\mathrm{CSL}} = |\uparrow\rangle \, x_{\uparrow,\mathrm{CSL}}(0) + |\downarrow\rangle \, x_{\downarrow,\mathrm{CSL}}(0) \xrightarrow{\text{Collapse}} |\uparrow\rangle * x_{\uparrow,\mathrm{CSL}}(\tau) = |\uparrow\rangle \tag{2.12}$$

How do the amplitudes fluctuate exactly? This can be derived via the Born rule, and is done in full in [8]. Here, we provide a brief overview: Let us measure the spin a hundred times ($N = 100$). According to the Born rule, we should get the outcome "up"

($|\uparrow\rangle$) exactly $x_\uparrow(0) * N$ times, whereas we should get outcome "down" the remaining $(1 - x_\uparrow(0)) * N$ times. In CSL theory, the fluctuations must hence chosen be such that we have

$$x_{\uparrow,\mathrm{CSL}}(0) \xrightarrow{\tau} 1 \tag{2.13}$$

for precisely $x_\uparrow(0) * N$ times. An analogy to this behavior is given by the "gambler's ruin game", and is due to Pearle [9]. Let us consider two gamblers, with CHF 100 between them. Gambler 1 starts with CHF $X_1(0)$, gambler 2 with CHF $X_2(0) = 100 - X_1(0)$. They toss a fair coin: "fair" is crucial, making the game what mathematicians call a *Martingale*. Heads, gambler 1 gives a dollar to gambler 2, tails, the reverse. This is a simple random walk in time, with probability to lose or gain a coin equal to 1/2. The amount each possesses at each time step t_k, $X_n(t_k)$, fluctuates. The game ends if one gambler is in possession of all the money. What is the probability that gambler 1 wins? If gambler 1 starts out with a fraction $x_1(0) = \frac{X_1(0)}{100}$ of the total amount of money, that is the *fraction* of repeated games he wins. This is precisely the behavior we want for our spin-2 system. Since the continuous limit of a discrete random walk is Brownian motion, the amplitudes $x_{\uparrow,\mathrm{CSL}}(t)$ follow a Wiener process. Just like a particular sequence of coin tosses, say "Up, Up, Down, Down, Up", of coin tosses leads to gambler 1 winning, a particular path of Brownian motion, denoted by $B(t)$ and sampled with probability [8]

$$P(B(t)) = \frac{1}{\sqrt{2\pi\lambda t}} e^{-B(t)^2/2\lambda t} \tag{2.14}$$

leads to amplitude $x_{\uparrow,\mathrm{CSL}}$ "winning". Here, λ is constant diffusion rate, and "sampled" means that we sample a particular path from the external, stochastic noise field that triggers the reduction process. If we happen to pick a different path, we get different fluctuations, and hence a different outcome. An overview of this process is given in Figure (2.2).

2.2.2. The modified Schroedinger equation

We are now in a position to understand the different modifications to the Schroedinger equation. Ghirardi & Bassi proposed the original modification to the Schroedinger equation to be [1] (equation 7.9 in their review)

$$d\,|\Psi(t)\rangle = -i\hat{H}dt + [\hat{A}dB(t) - \frac{1}{2}\lambda_{\mathrm{CSL}}\hat{A}^\dagger\hat{A}dt]\,|\Psi(t)\rangle \tag{2.15}$$

Here, $\hat{A}$ is the observable under consideration: If we want a collapse in the energy basis, we choose $\hat{A} = \hat{H}$, if we want a collapse in the momentum basis, we have $\hat{A} = \hat{p}$. Equation (2.15) is the standard Schroedinger equation with two modifications:

1. A diffusion term $\lambda_{\mathrm{CSL}}\hat{A}^\dagger\hat{A}dt$, where λ_{CSL} denotes the mean rate of diffusion, as such it can be interpreted similar to λ_{GRW} from the GRW model.

2. A stochastic term $\hat{A}dB(t)$ that enacts the amplitude fluctuations.

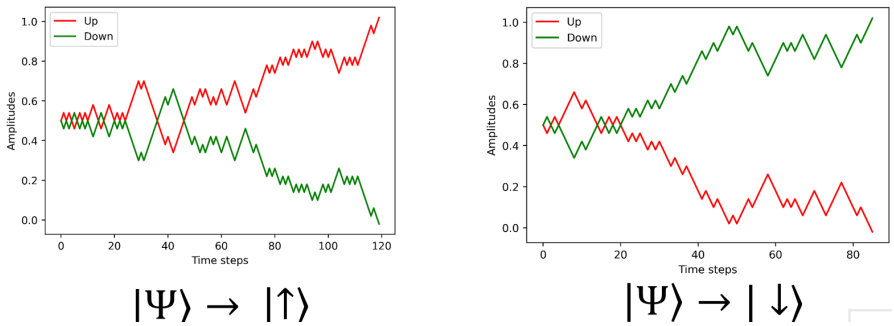

Figure 2.2.: Visualization of amplitude fluctuations. In CSL theory, the probability amplitudes are not constant in time, but flucutate due to interaction with an external noise field. The reduction process is complete once a given amplitude reaches unity value. Depending on the path of Brownian motion sampled from the noise field, the state vector $|\Psi\rangle$ gets reduced to one of its eigenstates $|\uparrow\rangle$ or $|\downarrow\rangle$.

The correct way to interpret the differential $dB(t)$ is via *Ito* calculus [4]. At its most basic level, Ito calculus is an extension of Riemann integrals to include stochastic processes, i.e. processes where the integration *measure* is random and distributed according to a Wiener process. If we evaluate equation (2.15) in the position basis, we get a stochastic differential equation for the wave function $\Psi(x,t) = \langle x|\Psi(t)\rangle$. Note that now each point in space x has a separate noise field assigned to it, such that equation (2.15) becomes

$$d\Psi(x,t) = -i\hat{H}dt + [\hat{A}dB(x,t) - \frac{1}{2}\hat{A}^\dagger\hat{A}\lambda dt]\Psi(x,t) \tag{2.16}$$

We can formally characterize the noise field $dB(x,t)$ via its correlation function and average values. Confirming that the we indeed have a Martingale process (that our gambler's ruin game is "fair"), we have

$$\langle dB(x,t)\rangle = 0 \tag{2.17}$$

The fields are correlated correlated at different points x, y in space

$$\langle dB(x,t)dB(y,t)\rangle = \lambda_{\mathrm{CSL}}\Phi(x-y)dt \tag{2.18}$$

where $\Phi(x-y)$ is the *correlator* that is Gaussian for the CSL model [4].

2.2.3. Collapse basis

One question left to address in the previous part is onto which *basis* the collapse process occurs, i.e. which operator $\hat{A}$ we have to choose. In the CSL model, this is solved via

introducing a locally averaged density operator [1]

$$\hat{N}(\vec{x}) = \sum_s \int \Phi(\vec{y} - \vec{x}) \hat{a}^\dagger(\vec{y}, s) \hat{a}(\vec{y}, s) d\vec{y} \tag{2.19}$$

Here, $\hat{a}^\dagger(\vec{y}, s)\hat{a}(\vec{y}, s)$ are, respectively, the creation and annihilation operators of a particle in space point $\vec{y}$ with spin s, and Φ is the Gaussian correlator defined above. It is given by

$$\Phi(\vec{x}) = \left(\frac{1}{\sqrt{2\pi r_c}} \right)^3 e^{-\vec{x}^2/2r_c^2} \tag{2.20}$$

and denotes the volume over which we take the density average. As such, an initial state reduces to an eigenstate of the operator $\hat{N}(\vec{x})$, i.e. the collapse happens in the position basis. CSL theory hence addresses *spatial* superpositions. The parameter r_c gives the spread of the Gaussian volume over which we average, and corresponds to the localization length that was discussed in the GRW theory section. To account for different kinds of particles such as electrons or protons and their respective masses, we introduce the *mass* density operator [1]

$$\hat{M}(\vec{x}) = \sum_\alpha m_\alpha \hat{N}_\alpha(\vec{x}) \tag{2.21}$$

Here, the index α labels the different particle species, $\hat{N}_\alpha(\vec{x})$ is the density operator for a particle of species α, and m_α is the mass of that particle species. The main motivation to replace the number density operator $\hat{N}(\vec{x})$ with the mass density operators $\hat{M}(\vec{x})$ derives from the desire to relate reductions to gravity (cf. Section (2.2.5)). A further benefit of this is that the collapse rates for microscopic systems are even further suppressed, leading to a smaller increase in energy and hence a smaller disagreement with SQD.

2.2.4. Operator formalism

While dynamical reduction is cumbersome to prove on the state level, it is comparatively easy to calculate CSL effects using the density operator formalism. The CSL evolution for the density operator $\hat{\rho}$ is given by [1]

$$\frac{d}{dt}\hat{\rho} = (\mathcal{L} + \mathcal{L}_{\text{CSL}})\hat{\rho} \tag{2.22}$$

where $\mathcal{L} = -\frac{i}{\hbar}[H, \rho(t)]$ is the standard Liouvillian and $\mathcal{L}_{\text{CSL}}$ is the CSL term given as

$$\mathcal{L}_{\text{CSL}} = -\frac{\lambda_{\text{CSL}}}{2r_c^3\pi^{3/2}m_0^2} \int d\vec{x}[\hat{M}(\vec{x}), [\hat{M}(\vec{x}), \hat{\rho}_t]] \tag{2.23}$$

with $\hat{M}(\vec{x})$ defined in equation (2.21), and $m_0 = 1\text{amu}$ a reference nucleon mass. What is the effect of the additional CSL term? According to our earlier reasoning, superpositions of different points in space should be suppressed, so we expect that the CSL term drives the off-diagonal elements of the density operator (in the position basis) to zero. This

is precisely what happens when doing the calculation. Let $\{|\vec{x}\rangle\}$ be the position basis, where for a system of N particles $\vec{x} = (\vec{x}_1, ..., \vec{x}_N)$. It can then be shown that for two particles (at positions $\vec{x}$ and $\vec{y}$) separated by $d = ||\vec{x} - \vec{y}|| \gg r_C$, we have [1]

$$\frac{\partial}{\partial t}\langle\vec{y}|\rho_t|\vec{x}\rangle = -\Gamma(\vec{x},\vec{y})\langle\vec{x}|\rho_t|\vec{y}\rangle \tag{2.24}$$

To give an expression for $-\Gamma(\vec{x},\vec{y})$ for different systems under consideration is the goal this report.

2.2.5. Gravitational collapse

One question left unanswered by the CSL model is the *origin* of the stochastic noise field $B(\vec{x},t)$. In 1989, Diosi proposed a modification to the GRW model with the explicit aim of eliminating the "new" constants of nature λ and r_c and of relating the process to gravity [5]. He established a modification to the Standard Schroedinger equation that can be related to CSL form. Instead of the Gaussian correlator $\Phi(\vec{x} - \vec{y})$ defined in equation (2.19), we choose a different correlator:

$$\Phi_{\mathrm{DP}}(\vec{x} - \vec{y}) = \frac{G}{\hbar}\frac{1}{|\vec{x} - \vec{y}|} \tag{2.25}$$

Here, G is the gravitational constant and the correlator has the typical form of a Newtonian potential. Besides this formal argument, Penrose [10] provided a more intuitive argument of why gravity could induce wavefunction collapse. He noted that when a system is in a spatial quantum superposition, a corresponding superposition of two different spacetimes is generated, as illustrated in Fig. (2.3). He then gave a minimalist argument [10] as to why nature "dislikes" and, therefore, suppresses superpositions of different spacetimes; the more massive the system in the superposition, the larger the difference in the two spacetimes and the faster the wave function collapse. Let us consider an example: Two rigid balls with radius R with well-defined mass distributions are in a quantum superposition

$$\Psi(\vec{x}, t = 0) = \psi_1(\vec{x}) + \psi_2(\vec{x}) \tag{2.26}$$

where ψ_1 and ψ_2 are two energy eigenstates with eigenvalues E_1 and E_2. The Diosi-Penrose criterion then predicts that gravity induces a collapse of this superposition after a time τ_{DP}

$$\tau_{DP} = \frac{\hbar}{\Delta E} \tag{2.27}$$

Here, ΔE is the difference in gravitational self-energy. It is given by

$$\Delta E = \frac{1}{G}\int dV\,(\nabla\Phi_1 - \nabla\Phi_2)^2 \tag{2.28}$$

where Φ_1 and Φ_2 are the Newtonian gravitational potentials of the two states. In a way,

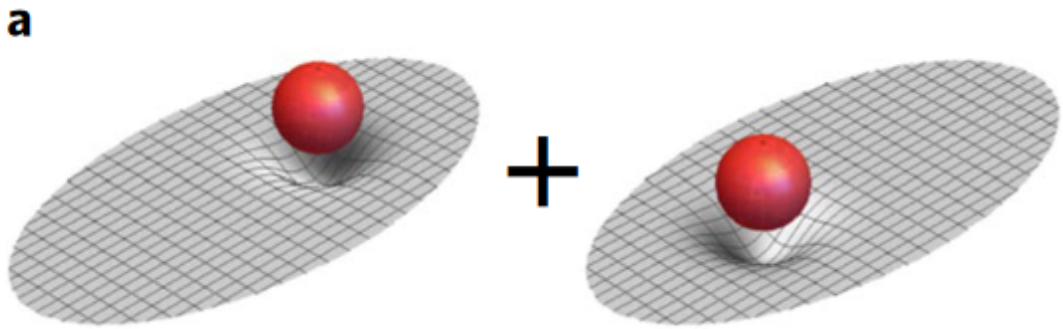

Figure 2.3.: According to quantum gravity, a spatial quantum superposition of a system (red sphere) generates a superposition of different spacetime curvatures (grey sheets), corresponding to the possible different locations of the system. Penrose argues that a superposition of different spacetimes is unstable and decays in time, making the system's wave function also collapse. Taken from [11]

.

ΔE measures how large, in gravitational terms, the superposition is. We calculate ΔE for our two balls and arrive at

$$\Delta E \approx G\frac{(E_1 - E_2)^2}{c^4 R} \tag{2.29}$$

such that the superposition is destroyed after a time

$$\tau \approx \frac{c^4 \hbar R}{G(E_1 - E_2)^2} \tag{2.30}$$

There is an argument by Gao [12] showing that this collapse time may be inconsistent with the discreteness of space-time. In addition, a recent experiment in the Gran Sasso underground laboratory has further questioned the validity of the DP model: The particles, which are accelerated by the collapse noise, emit radiation if charged. This emitted radiation can be detected and allows to place bounds on the DP parameters. A corresponding experiment was done by Donadi et al. in 2020 [11].

2.2.6. Interpretation as stochastic potential

Another useful way to imagine the effect of the CSL noise field on a particle is by considering the following modified Schroedinger equation

$$\frac{d}{dt}\left|\Psi\right\rangle = (\hat{H} + \hat{V}(t)_{CSL})\left|\Psi\right\rangle \tag{2.31}$$

where we added a stochastic potential to the standard Schroedinger equation that is given as

$$\hat{V}(t)_{CSL} = \frac{\hbar\sqrt{\lambda}}{\pi^{3/4} r_C^{3/2} m_0} \int \frac{d\vec{x}}{dt} \hat{M}(\vec{x}) dB(\vec{x}, t) \tag{2.32}$$

Here, $B(\vec{x}, t)$ denotes the same stochastic noise field as above. This modified equation yields the correct time evolution equation for the *density* operator, and was introduced by Bassi [13]. Why is this useful? The stochastic potential appears as a stochastic force in the quantum Langevin equations. For example, we have for the momentum operator $\hat{p}$

$$\hat{F}_{CSL}(t) = \frac{i}{\hbar}[\hat{V}_{CSL}(t), \hat{p}] \tag{2.33}$$

This provides an intuitive way to understand why the stochastic field $B(\vec{x}, t)$ leads to momentum diffusion: The particles get repeatedly kicked by the noise, similarly to diffusion due to thermal noise. Besides this violation of energy conservation, another weak point of CSL theory is the spectrum of the noise, which is flat. If one thinks that the noise providing the collapse has a physical origin, it cannot be white but colored, with a cut off. For this purpose, the *colored* CSL model has been developed [14].

Chapter 3

Test of collapse models

Contrary to most other proposed solutions of the measurement problem, collapse models are experimentally testable. Experiments testing the CSL model can be divided in two classes: interferometric and non-interferometric experiments, which respectively probe direct and indirect effects of the collapse mechanism. From now on, we also leave out the subscript "CSL" when refering to the collapse rate λ.

3.1. Interferometric experiments

Interferometric experiments can detect the direct action of the collapse, which is to localize the wavefunction in space. They include all experiments where a spatial superposition is generated and, after some time, its interference pattern is probed. If interference fringes appear, the superposition principle holds for that type of system within the measurement error; otherwise, it is violated. This can be due to different reasons, such as localization of the system's wavefunction predicted by a collapse model. In particular, the action of CSL is quantified by the reduction of the off-diagonal terms of the statistical operator. Experiments testing such a reduction are carried out with cold-atoms [15], molecules [16] and entangled diamonds [17]. One drawback of interferometric experiments is that preparing and maintaining spatial superpositions of massive systems over time is challenging from a technical perspective as it requires isolation from any external agent. Typically, this requires low temperature, high vacuum and low-vibration conditions. State-of-the-art interferometric experiments now employ particles of around 104 atomic mass units and have set an upper bound of $\lambda \ll 10^{-7}\ s^{-1}$ at $r_C = 10^{-7}$ m for the CSL model [18]. This is a billion times weaker than what is needed to probe the GRW value.

3.2. Non-interferometric experiments

Non-interferometric experiments are not based on the preparation of a superposition, but exploit the momentum diffusion induced by the interaction with the collapse noise. As outlined in Section (2.2.6), the effect of the noise amounts to an effective stochastic force acting on the system, and several experiments can be designed to quantify such a force. As the typical strength of the collapse rate is very small, a successful experiment will still have to suppress other noise sources from the environment. Non-interferometric tests include radiation emission from charged particles [19], heating in bulk materials [20], and diffusive effects. Most experiments that exploit diffusive effects aim to measure

the increase of the spread in position of center-of-mass of a system. The strategy is then to monitor the motion of the particle in a controlled environment, looking for Brownian fluctuations that would signal the onset of CSL-induced effects. Conversely, the *lack* of such a detection would place *upper* bounds on the collapse parameters λ and r_c. Similar relations can be obtained for cold-atom experiments, opto-mechanical systems [21][22], and gravitational wave detectors [13]. Combined, they allow one to draw the so-called exclusion plots that identify the regions of parameters that need to be explored to rule out a given collapse model. Figure (3.1) reports the most current exclusion zone plot.

3.3. Examples

We have outlined (cf. Section (2.2.4)) that the CSL model leads to a modified time evolution for the density operator given by

$$\frac{d}{dt}\hat{\rho}_t = (\mathcal{L} + \mathcal{L}_{\mathrm{CSL}})\hat{\rho} \tag{3.1}$$

A whole body of literature is devoted to find explicit expressions for the Lindblad term $\mathcal{L}_{\mathrm{CSL}}\hat{\rho}$ using many different experimental setups. We provide two examples below.

3.3.1. Cantilever tests

Let us focus first on cantilever configurations, where the center of mass of a rigid body of mass m oscillates linearly, say, along the x axis with an amplitude $x_0 \ll r_c$. This could be a cubic mirror, an optically trapped nanosphere, or a micromembrane. The Lindblad term is then given by [21]

$$\mathcal{L}_{\mathrm{CSL}}\hat{\rho} = -D_{CSL}[\hat{x}, [\hat{x}, \hat{\rho}]] \tag{3.2}$$

with $\hat{x}$ the center-of-mass position operator and $D_{CSL} = \frac{\lambda}{r_c^2}\alpha$. The factor α depends on the geometry oscillator and can be caluclated for simple configurations [21]. How can this place bounds on the CSL parameters? The stochastic noise force kicks the particle with a force proportional to D_{CSL}, leading to momentum diffusion. This momentum diffusion would dominate over diffusion from thermal noise that "kicks with force D_T" (and would thus be detectable in a noise spectrum), if $D_{\mathrm{CSL}} > D_T$. By solving this equation for λ, bounds on its value can be obtained. This idea, here presented at a very basic level, can be extended to all kinds of systems: Gravitational wave detectors [13], rotational opto-mechanics [6], and further cantilever-based experiments [23] [24].

3.3.2. Direct tests

Direct tests don't rely on noise spectra to place bounds on the CSL parameters, but use a "brute-force" approach instead. The goal is to derive an explicit expression for equation (2.24), i.e. to derive an expression for the decay rate $\Gamma(\vec{x}, \vec{y})$. To do so, we first simplify the CSL term $\mathcal{L}_{\mathrm{CSL}}\hat{\rho}$. Next, we choose appropriate basis kets $|\vec{x}\rangle$ and $|\vec{y}\rangle$ and project the simplified Liouvillian onto this basis. This yields the desired decay rate $\Gamma(\vec{x}, \vec{y})$, which

subsequently allows us to place bounds on the CSL parameters. As an example, consider a system where the off-diagonal elements decay exponentially in time

$$\langle \vec{x}|\rho_t|\vec{y}\rangle = \langle \vec{x}|\rho_0|\vec{y}\rangle e^{-D_{\mathrm{CSL}}(\lambda,r_c)t||(\vec{x}-\vec{y})||} \tag{3.3}$$

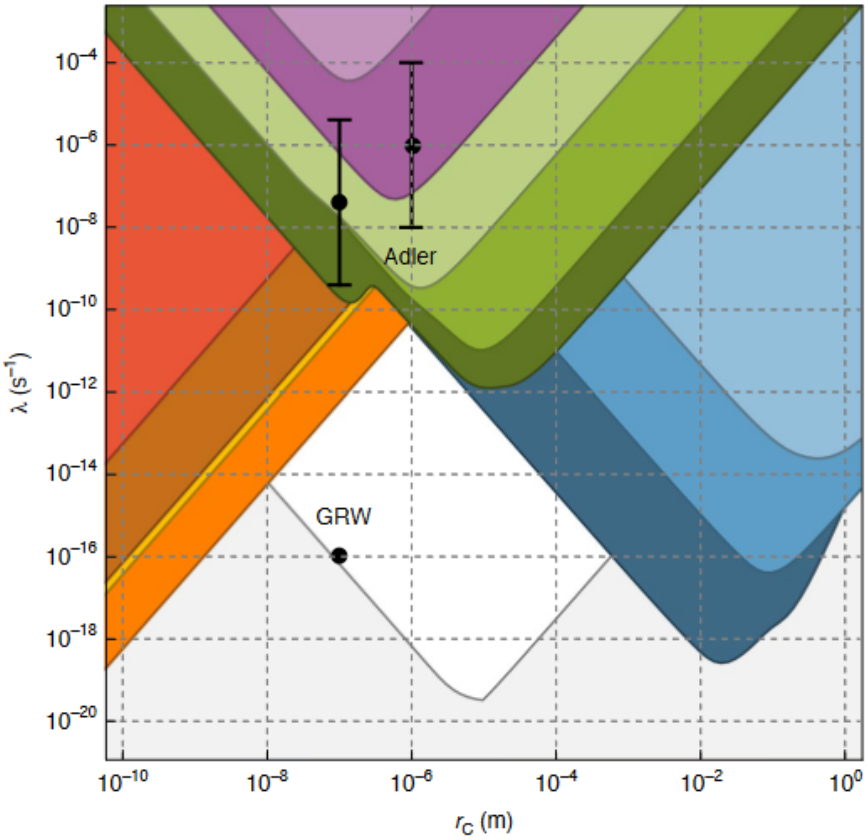

Figure 3.1.: *Exclusion plot for CSL parameters λ and r_c from non-interferometric tests.* The coloured areas correspond to experimentally excluded regions. The green-coloured regions are from cantilever-based experiments. The blue areas are obtained from gravitational wave detectors. The purple areas are from optomechanical systems levitating in a linear Paul Trap and a magnetic trap. The orange area is from spontaneous X-ray emission tests. The yellow area is from phonon excitation in the CUORE experiment. The brown area is calculated from heating rates, and the red area is drawn from cold-atom experiments. The theoretical values proposed by GRW and the ranges proposed by Adler are shown as a black dot and black dots with bars that indicate the estimated range, respectively

Here, D_{CSL} is a function of the collapse paramters λ and r_c, and sets the strength of the decay. Its explicit form will be given in a later section. If, after a time τ, there is an interference pattern (the superposition hasn't collapsed), the following relation must hold:

$$D_{\mathrm{CSL}}(\lambda, r_c)||(\vec{x} - \vec{y})||\tau \ll 1 \tag{3.4}$$

The approach to calculate exclusion zones is then as follows: We first find an explicit expression for $D_{\mathrm{CSL}}(\lambda, r_c)$. This expression changes for different experimental setups, and can only be calculated in closed form for a selected few setups. In a next step, the above inequality is evaluated for each pair (λ, r_c) in parameter space. Both steps are shown in detail in the following sections.

3.4. Experimental setups

We present two experimental setups that may be used for direct CSL tests. This first one, which we call the *diamond* configuration, was proposed by Lee et al. [17], and is illustrated in Figure (3.2*a*). The core consists of two 0.25 mm thick diamonds that are a distance d apart. Using an ultrashort laser pulse split by a beam-splitter, a single phonon in a mode with frequency $\omega = 40 * 10^9\ s^{-1}$ is excited with probability $P_e \ll 1$ via a Stokes process. After the *pump* pulse, the entanglement is verified with a *probe* pulse

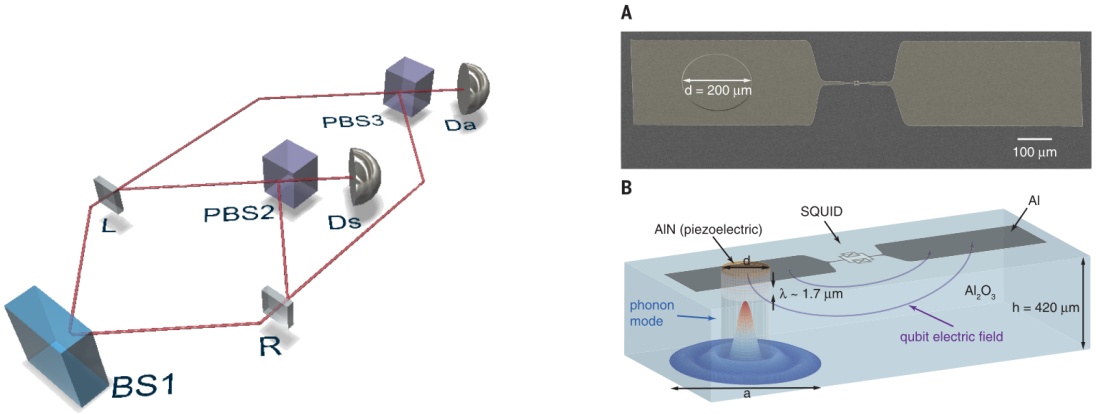

a The diamond setup.

b The sapphire setup.

Figure 3.2.: Comparison of two experimental setups *A*: Entanglement of two phonon modes in diamond. A pump pulse split by a mirror (BS1) hits two diamonds normal to their surface and excites a phonon via a Stokes process. The detector D_S detects the Stokes process, the detector D_A confirms the entanglement via detecting the higher-frequency Anti-Stokes photon Taken from [25]. *B*: A HBAR on top of a slab of sapphire. The phonon volume is plotted in inset B. It gets excited via piezoelectric coupling to the Transmon. Taken from [26].

emitted a time τ after the pump pulse. Note that τ must be smaller than the phonon lifetime of $\gamma^{-1} = 7 * 10^{-12}$ s. Intuitively, the probe pulse maps the phonon state to a photon state via an Anti-Stokes process. We summarize the most important parameters of the experiment below:

1. Superposition lifetime $\tau = 350 * 10^{-15} s$.
2. Phonon frequency $\omega = 40 * 10^9$ s^{-1}
3. Diamond mass density $\rho = 3.51$ g/cm^3
4. Molar mass $M = 12.01$ g/mol
5. The laser beam hits the diamond normal to its surface. The cross section of beam and diamond is hence a cylinder, where the cylinder height is equal to the diamond thickness $d = 0.25$ mm and the diameter is the beam width, $R = 3.6\mu m$. As such, the effective phonon volume is roughly given by $V = \pi R^2 * d$.

As we consider a single mechanical mode of two diamonds, we may describe the entangled state in terms of the Fock basis $\{|n\rangle \otimes |m\rangle\}$. Labelling the left and right diamond by L and R, respectively, it can be shown [25] that the entangled state can be written as

$$|\Psi\rangle = \sqrt{\frac{1}{2}} \left(|n_L = 1, n_R = 0\rangle + |n_L = 0, n_R = 1\rangle\right) \tag{3.5}$$

For the present discussion, we restrict ourselves to a single excitation ($n_L \leq 1, n_R \leq 1$), such that the resulting Hilbert space has dimension $d = 4$. We want to re-create an identical state using a different experimental setup, in order to get different parameters (e.g. a longer superposition time). One possible setup yielding an identical state is illustrated in Figure (3.2*b*). It employs two HBARs (high overtone bulk acoustic wave resonators) fabricated using a slab of sapphire. We call this experiment the *sapphire* setup. We briefly explain the setup below, with detailed information in [26], [27]: Piezoelectric crystals are attached on top of the sapphires, which deform when placed in an electric field. Here, the electric signal comes from a superconducting transmon qubit. The vibration generated by periodic deformations in the piezo crystal is passed on to the sapphire, which can store it as an acoustic standing wave, i.e. a phonon. If the HBAR is cooled close to absolute zero, the high-frequency mechanical modes are in the ground state, and it becomes possible to excite and control individual phonons. Compared to the diamond setup, we have an identical state $|\Psi\rangle$, but with different parameters listed below:

1. Superposition lifetime $\tau = 50 * 10^{-6} s$. The lifetime is hence much longer than for the diamond experiment.
2. Phonon frequency $\omega = 6 * 10^9$ s^{-1}. This is one order of magnitude lower than in the previous experiment.

3. Sapphire mass density $\rho = 3.98\ g/cm^3$, which is similar to diamond.

4. Molar mass $M = 101.96\ g/mol$, which is one order of magnitude higher than for diamonds.

5. The phonon volume is a cylinder, this time with height $d = 0.4mm$ and radius $R = 12.5\mu m$.

3.4.1. Phonon mass

The displacement of the atoms that make up the phonon is related to the zero-point fluctuations (ZPF) of the given phonon mode. To determine the ZPF, we require knowledge of the oscillator mass, which is not straightforward to determine. In the main reference paper [25] of this semester report, the authors reference *private* communication to conclude that the oscillator mass m^* is given by $m^* = 6u$ for the diamond experiment, where u is the atomic mass unit (AMU). This is exactly half of the mass $m = 12u$ of a carbon atom, and is likely because they consider optical phonons, where the atoms per unit cell counter-oscillate, such that the number of atoms contributing to the phonon is halved. We question this reasoning and provide an alternative calculation. To do so, we consider the effective phonon volume V as well as the number density of the oscillator material (diamond or sapphire), denoted by n. From these values, we determine the number $N = nV$ of atoms contributing to the phonon. The phonon mass is then given by $m = m_A N$, where m_A is the mass of a single atom (e.g. carbon in diamond). We hence define

$$m_{\mathrm{PH}} = m_A * n * V \tag{3.6}$$

and use m_{PH} instead of m^* in our following calculations. For the two experimental setups introduced above, we use the following values for m_A and the number density n:

1. For diamonds, we have carbon mass $m_A = 12u$, and number density $n = 176.29\ 10^{27}\ m^{-3}$. This leads to $m_{PH} = 3.56\ 10^{-11}$ kg.

2. Since sapphire is a compound, we calculate the atom mass using its molar mass: $m_A = \frac{M_{mol}}{\mathcal{N}_A}$, where $\mathcal{N}_A$ is the Avogadro constant. This yields $m_A = 101.96u$. The number density can be calculated by using $n \approx \frac{\rho}{m_A}$, giving $n = 2.35\ 10^{28}\ m^3$. We check the formulas presented here by inserting the values for the diamond experiment. Doing so, we get the identical values as in our reference paper [25], confirming the valditiy of this approach. In summary, we have $m_{PH} = 7.83\ 10^{-10}$ kg for the sapphire setup.

We thus have an updated oscillator mass for each setup. To complete the analysis, we also provide a value m^* for the sapphire setup following the "wrong" approach as in reference paper [25]. The main difference is that instead of optical phonons, we excite *longitudinal* phonons in the sapphire. This leads to $m^* = 101.96u = m_A$, compared to $m^* = 6u$ for the diamond setup.

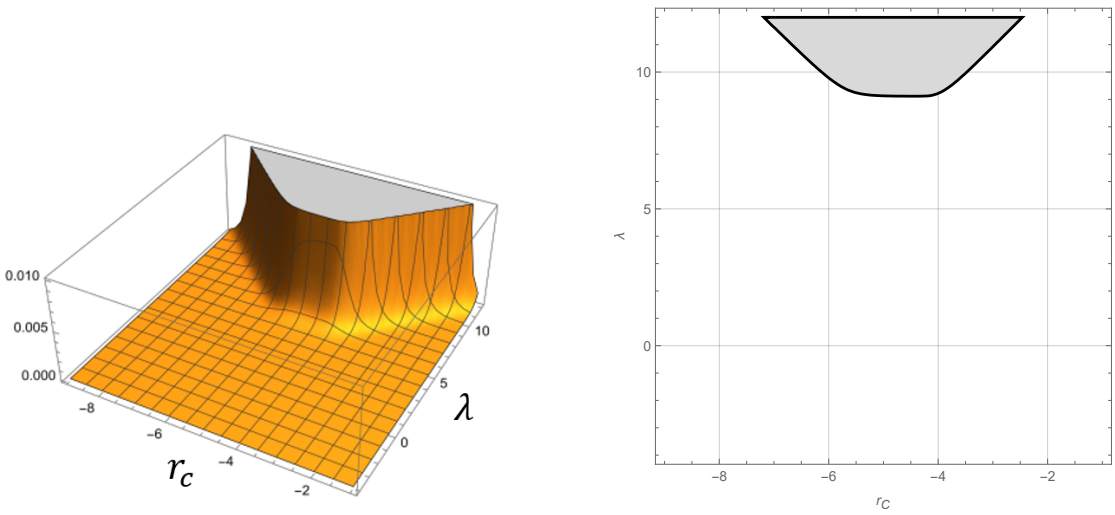

a 3D exclusion zone plot.

b 2D exclusion zone plot.

Figure 3.3.: Visualization of parameter exclusion zones. *A*: Plotted is the numerical value of Γ evaluated at different tuples (λ, r_C) on a log-log scale. Here, $\lambda \in [10^{-4}, 10^{10}]$ (vertical basegrid axis) and $r_C \in [10^{-9}, 10^{-1}]$ (horizontal basegrid axis). To evaluate inequality (3.9), we choose a cut-off $c = 0.01$. The bowl-shaped plateau indicates the coordinate subspace for which the inequality is invalid. *B*: 2D plot of the same setup, i.e. we look at plot (A) form a bird's eye view. The light gray area denotes the parameter subspace which contradicts experimental results.

3.4.2. Relevance of CSL effects

We previously highlighted that the CSL amplification mechanism relies on center-of-mass (COM) motion. However, in the experiments discussed here, the COM is always well localized, such that is a priori unclear if CSL dynamics are involved at all. Considering the superposition state $|\Psi\rangle$ for the diamond setup, the phonon cannot be assigned to either the left or right diamond. Hence, the relevant superposition of matter is *within* each diamond (atoms at rest vs. atoms oscillating), not *between* the two diamonds. The separation distance of the diamonds does thus not play a role at all when considering CSL effects.

3.5. Updated exclusion zone plots

We will show in detail in Section (4) that the decay rate $\Gamma(\vec{x}, \vec{y})$ at a time τ is given by

$$\Gamma(\vec{x}, \vec{y}) = -2\beta\tau D^*_{\mathrm{CSL}}(r_c)(x_{\mathrm{ZPF}})^2\lambda \tag{3.7}$$

where β is a factor that depends on the type of phonon under consideration. Note that we have

$$D^*_{\mathrm{CSL}}(r_c) * \lambda = D_{\mathrm{CSL}}(r_c, \lambda) \tag{3.8}$$

i.e. we have *linear* scaling in the collapse rate λ. Upper bounds on both collapse parameters are obtained by solving the inequality

$$\Gamma(\vec{x}, \vec{y}) \leq c \tag{3.9}$$

where c is a constant much smaller than 1, $c \ll 1$, following the reasoning from equation (3.4). This inequality is evaluated numerically using Mathematica. We undertake the following steps to obtain exclusion zones:

1. We specify a parameter range for both λ and r_c, such that we have a 2D parameter grid. We then evaluate inequality (3.9) for each coordinate tuple (λ, r_c) of the parameter grid. If the inequality evaluates to True, λ and r_c are valid parameters that don't violate any experimental results. If not, the tuple under consideration is ruled out.

In Figure (3.3), we plot the numerical value of $\Gamma(\vec{x}, \vec{y})$ for each set of parameter coordinates (λ, r_c), where we have set a cut-off $c = 0.01$. The coordinate tuples (λ, r_c) for which the above evaluates to "False" are colored in Light Gray in Figure (3.3*b*). This yields the exclusion zone. Next, we compare the exclusion zones for both experimental setups. In addition, we compare the decay rate calculated using the correct value for the oscillator mass, m_{PH}, with the one in the reference paper [25] using m^*, such that we have two exclusion zones for both setups. This yields *four* new exclusion zones, all of which are illustrated in Figures (3.4*b*) and (3.5).

Interpretation

Naturally, we expect the bounds on the parameters placed using m_{PH} to be smaller than in [25] since the value of $\Gamma(\vec{x}, \vec{y})$ obtained when using the updated phonon mass is much smaller. To quantify the difference, we note that $\Gamma(\vec{x}, \vec{y}) = -2\beta\tau D^*_{\mathrm{CSL}}(r_c)(x_{\mathrm{ZPF}})^2 * \lambda$ has the proportionality (cf. Chapter 4)

$$\Gamma \propto m_{\mathrm{PH}} \tag{3.10}$$

when using the updated oscillator mass, whereas it is proportional to

$$\Gamma \propto m^2_{\mathrm{PH}}/m^* \tag{3.11}$$

when using the *wrong* oscillator mass used in [25]. The factor $\gamma = m_{PH}/m^*$ quantifies the difference in exclusion zones. For the diamond setup, we find $\gamma \approx 3.6 * 10^{-15}$, whereas for the sapphire setup we have $\gamma \approx 4.7 * 10^{-15}$. As such, for both setups, the value of the decay product Γ is about 15 orders of magnitude smaller in the correct approach when compared to the calculation in [25] using m^*. Due to the linear scaling of Γ with

λ, i.e. $\Gamma \propto \lambda$, we expect the exclusion zones to be approximately identical in shape, but displaced along the vertical (the λ) axis by γ. Intuitively speaking, λ has to make up the 15 orders of magnitude that we lose when using the updated oscillator mass.

Looking at the results, we do *not* obtain any new excluded paramter regions. This is sensible since the superposition of matter is within each diamond, and the separation distances involved are very small (on the order of x_{ZPF}). In addition, the superposition time is very small as well, such that the value of the product Γ is negligible even though the number of atoms that contribute to the phonon is large.

A second instructive comparison is between the sapphire setup and the diamond setup, once using m^* and once using m_{PH}. For this, note that Γ is linearly proportional to the superposition time

$$\Gamma(\tau) \propto \tau \tag{3.12}$$

Since we have $\frac{\tau_D}{\tau_S} \approx 10^{-8}$, we expect the exclusion zone for diamond to be displaced along the λ axis by approximately 8 orders of magnitude compared to the sapphire one using the same reasoning as above. The remainder can be attributed to differences in phonon volume V and frequency ω. This is confirmed when looking at Figures (3.5) and

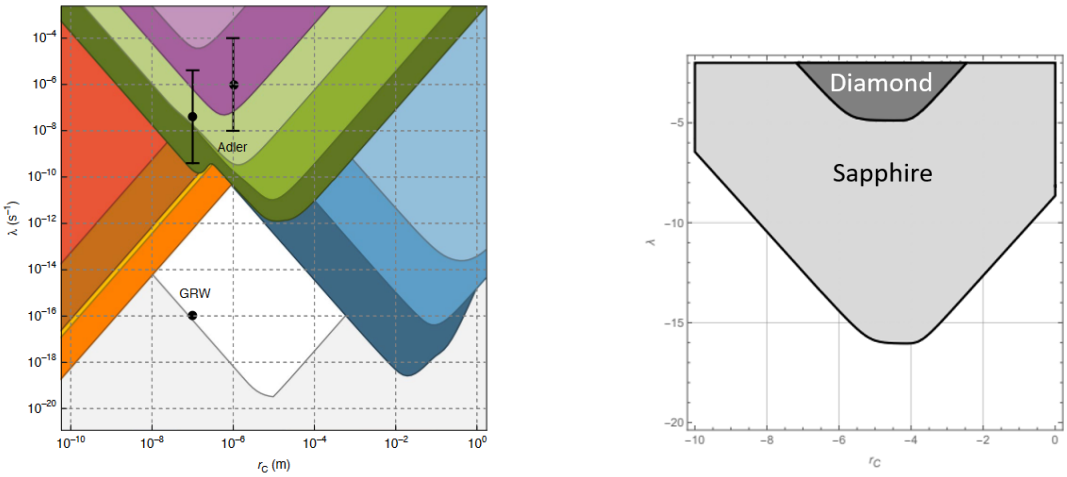

a Left b Right

Figure 3.4.: Visualization of parameter exclusion zones. *A*: Most recent exclusion zone plot, described in detail in Section (3). Taken from [28]. *B*: Exclusion zone plot for both the diamond (Dark Gray) and HBAR (Light Gray) experimental setups, obtained when following the "incorrect" calculation in [25]. A log-log scale is used. The values of the parameters $T, R, D, \omega, m_{\mathrm{PH}}$, and m^* are given in Section (3.4). Confirming our remarks in the text, we find a order of magnitude difference between diamonds and HBARs of about 10^{-10}, with the remainder attributed to differences in phonon volume (different radius and thickness). The Light gray area would indeed predict novel bounds on the CSL parameters.

(3.4*b*).

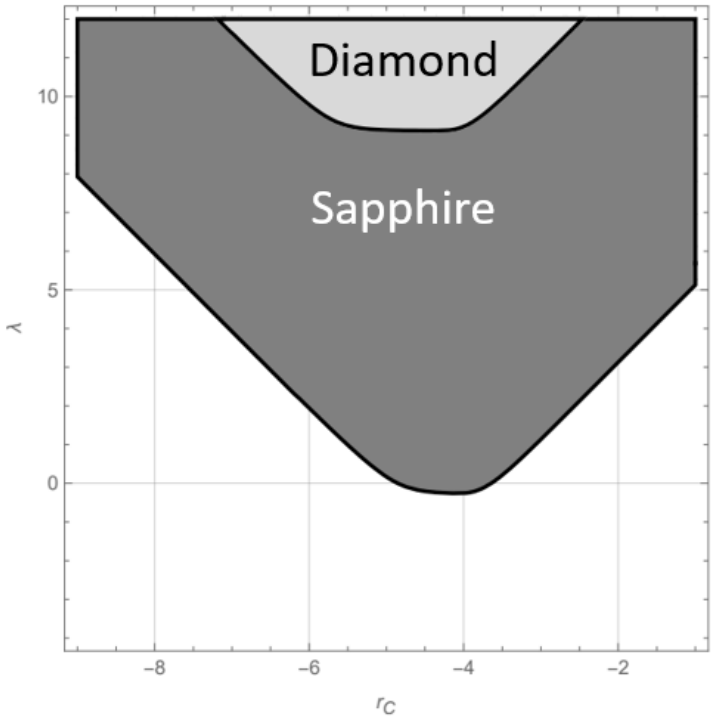

Figure 3.5.: Exclusion zone plot for both the diamond (Light Gray) and HBAR (Dark Gray) experimental setups, obtained using the calculation presented here. A log-log scale is used. The values of the parameters $T, R, D, \omega, m_{\mathrm{PH}}$, and m^* are given in Section (3.4). We again find a order of magnitude difference between diamonds and HBARs of about 10^{-10}, similar to Figure (3.4*b*). The different shapes are attributed to differences in phonon geometry (R, d). We are into the *positive* regime for λ, and don't obtain any new bounds.

Chapter 4

Explicit calculation of reduction rate

In this section, we explicitly want to calculate the decay rate $\Gamma(\vec{x}, \vec{y})$. By doing so, we provide closed-form expressions for $D_{\mathrm{CSL}}(\lambda, r_C)$, and simplify the CSL Liouvillian $\mathcal{L}_{\mathrm{CSL}}\hat{\rho}$. Following standard literature [13], [24], [23], we first linearize the mass density operator $\hat{M}(\vec{x})$ [25]

$$\hat{M}(\vec{x}) = \sum_n m_n e^{-(\vec{x}-\hat{\vec{x}}_n)^2/2r_c^2} \tag{4.1}$$

Note that the index n labels only nucleons and not electrons, as the mass of the latter is negligible compared to the nucleon mass. The position operator $\hat{\vec{x}}_n$ describes the displacement of a single particle n from its equilibrium position. To linearize the mass density operator, we note that the displacement of the atoms from their equilibrium position is minimal, i.e. $\delta x \ll 1$. This allows us to expand the position operator. We denote the (classical) equilibrium position by $\vec{x}^{(0)}_{n,\alpha}$, where the index α is necessary for optical phonons and describes if the atom belongs the either the sublattice oscillating in phase or out-of phase. This is illustrated in Figure (4.1). The displacement of a particle due to a phonon may be described by a quadrature operator $\hat{\vec{x}}_\alpha$:

$$\hat{\vec{x}}_\alpha = x_{\mathrm{ZPF}}(\hat{b} + \hat{b}^\dagger) \tag{4.2}$$

where $\hat{b}$ and $\hat{b}^\dagger$ are the phonon creation and annihilation operators, respectively. Note that there is no particle index n here as we employ the so-called rigid-body approximation [13], and hence all particles assigned to sub-lattice α are displaced identically. Since we consider only a *single* direction of excitation, simplifying the quadrature operator to $\hat{\vec{x}}_\alpha = (0, 0, \hat{z}_\alpha)$. We further note that for two counter-oscillating atoms labelled by a and b that move at the same frequency, we have $z_a = -z_b$, and as such

$$\hat{z}_{L_1} = -\hat{z}_{L_2} = \hat{q}_L \tag{4.3}$$

which also holds for the index R. Combining all these assumptions, we write the position operator $\hat{\vec{x}}_n$ as:

$$\hat{\vec{x}}_n = \vec{x}^{(0)}_{n,\alpha} + \hat{\vec{x}}_\alpha \approx \vec{x}^{(0)}_{n,\alpha} + \hat{q} \tag{4.4}$$

Using $\sum_n = \sum_\alpha \sum_{n\in A_\alpha}$, this leads to

$$\hat{M}(\vec{x}) = \sum_\alpha \sum_{n\in A_\alpha} m_n e^{-[\vec{x}-(\vec{x}^{(0)}_{n,\alpha}+\hat{\vec{x}}_\alpha)]^2/2r_c^2} \tag{4.5}$$

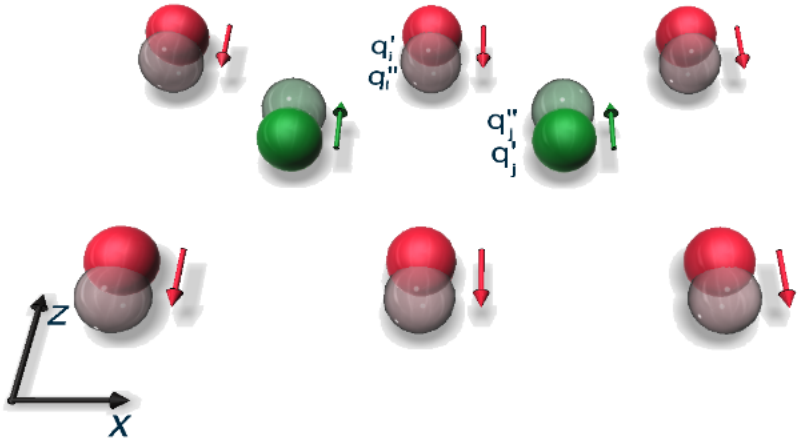

Figure 4.1.: Schematic representation of the displacements of carbon atoms in one diamond. The two different colors represent the two different counter-oscillating sublattices. Full colors denote the two sublattices at rest, while faded ones represent the two sublattices at the maximum relative distance.

How do we relate this expression involving a discrete collection of microscopic nuclei to the phonon geometry (the cylinder) outlined in Section (3.4)? Following [21], we assume a constant, continuous mass distribution $\mu(\vec{r})$ for both the diamond and the HBAR. With phonon volume V, we then have

$$\mu(\vec{r}) = \begin{cases} \frac{m}{V}, & \text{if } \vec{r} \in V \\ 0, & \text{otherwise} \end{cases}$$

where m is the sum of all individual nucleon masses in volume V that contribute to the phonon. This assumption is valid if the dimensions of the phonon volume V exceed the localization length, i.e. if $R \gg r_C$ and $d \gg r_C$. Next, consider that the mass of either sapphire or diamond is mainly concentrated in the nuclei located at $\vec{x}^{(0)}_{n,\alpha}$, i.e. its mass density is a discrete distribution of spheres of nuclear size. Since nuclei are extremely small with respect to other distances involved in the collapse process, the mass distribution can be considered as discrete. This approximation is often implicitly assumed in the literature. For an in-depth discussion on the validity of this assumption, see [29]. We can hence write

$$\mu(\vec{r})_\alpha = \frac{m}{V} = \sum_n m_n \delta^{(3)}(\vec{r} - \vec{x}^{(0)}_{n,\alpha}) \tag{4.6}$$

where the the index $\mu(\vec{r})_\alpha$ reflects that we make the generalization "discrete $\rightarrow$ continuous" independently for every atom lattice. We thus obtain a mass density operator than

can be related to the material densities used in experiment via

$$\hat{M}(\vec{x}) = \sum_{\alpha} \int_V d\vec{r} \mu(\vec{r})_\alpha e^{-(\vec{x}-\hat{\vec{x}}_\alpha-\vec{r})^2/2r_c^2} \tag{4.7}$$

The final step in simplifying $\hat{M}$ is to expand the exponential operator up to first order in $\hat{\vec{x}}_\alpha$, which is valid if $||\hat{\vec{x}}_\alpha|| \ll |\vec{x}|, |r|$. For this purpose, we introduce the functional $g(\hat{\vec{x}}_\alpha) = e^{-(\vec{x}-\hat{\vec{x}}_\alpha-\vec{r})^2/2r_c^2}$ and expand to first order, yielding

$$g(\hat{\vec{x}}_\alpha) \approx g(0) + \nabla g(\hat{\vec{x}}_\alpha)|_{\hat{\vec{x}}_\alpha=0} \hat{\vec{x}}_\alpha \tag{4.8}$$

We evaluate the second term containing the derivative:

$$\nabla g(\hat{\vec{x}}_\alpha)|_{\hat{\vec{x}}_\alpha=0} = \exp\{-(\vec{x}-\vec{r})^2/2r_c^2\} \frac{-2(\vec{x}-\vec{r})}{2r_c^2} \nabla(\vec{x} - \hat{\vec{x}}_\alpha - \vec{r})|_{\hat{\vec{x}}_\alpha=0} \tag{4.9}$$

Given that all $\hat{\vec{x}}$s commute with each other, they can be treated as plain vector variables, such that $\nabla(\vec{x} - \hat{\vec{x}}_\alpha - \vec{r})|_{\hat{\vec{x}}_\alpha=0} = I$ and hence

$$\begin{aligned} &\exp\Big\{-(\vec{x} - \hat{\vec{\alpha}} - \vec{r})^2/2r_c^2\Big\} = \\ &\qquad = \exp\{-(\vec{x}-\vec{r})^2/2r_c^2\} - \exp\{-(\vec{x}-\vec{r})^2/2r_c^2\} \frac{(\vec{x}-\vec{r})}{r_c^2} \hat{\vec{x}}_\alpha \end{aligned} \tag{4.10}$$

Inserting (4.10) into (4.7) gives

$$\hat{M}(\vec{x}) = M_0(\vec{x}) + \sum_{\alpha} \int \frac{d\vec{r}}{r_c^2} \mu(\vec{r})_\alpha e^{(\vec{x}-\vec{r})^2/2r_c^2} (\vec{x}-\vec{r}) \hat{\vec{x}}_\alpha \tag{4.11}$$

where we deliberately didn't write out the first term as it doesn't contain an operator anymore, and hence the the double commutator in definition (2.23) vanishes. We thus have our linearized description. In Appendix A, we show how inserting the linearized mass density operator (4.11) into the CSL density term (2.23) leads a similar equation as in the cantilever experiments (cf. Section (3)):

$$\frac{d}{dt}\rho_t = -\frac{i}{\hbar}[H, \rho_t] - \sum_{\alpha} D^{\alpha}_{\mathrm{CSL}}[(\hat{z}_\alpha)[(\hat{z}_\alpha), \rho_t]] \tag{4.12}$$

Here, the index α emphasizes that we might have different diffusion rates for different atom lattices. As it turns out (and as also makes sense), the two lattices (for optical phonons) have identical diffusion rates (they are symmetric after all). We thus use $D^{\alpha}_{\mathrm{CSL}} = D_{\mathrm{CSL}}$ for the remainder of the section. The closed-form expression for D_{CSL} (in position space) is provided in Appendix A as well, but is difficult to evaluate. We are hence led to perform a similar approach (linearize M, simplify, write down D_{CSL}) in *momentum* space. This yields the same equation as (4.12), but with a different, and

much more simple expression for D_{CSL}:

$$D_{\mathrm{CSL}} = \frac{\lambda r_c^3}{2m_0^2\pi^{3/2}} \int d\vec{k} e^{-r_c^2 k^2} |\mu(\vec{k})|^2 k_z^2 \tag{4.13}$$

Here k are polar momentum variables. The detailed calculation that leads to (4.13) is reported in Appendix B. It hence remains to calculate $|\mu(\vec{k})|$ to obtain an expression for D_{CSL}, which is done in Appendix C. Finally, we get

$$D_{\mathrm{CSL}}(\lambda, r_C) = \lambda \frac{m^2}{d^2 m_0^2} \Gamma_\perp \left(\frac{R}{\sqrt{2} r_c} \right) \left(1 - e^{-d^2/4r_c^2} \right) \tag{4.14}$$

Here, $\Gamma(x)$ is given by (cf. Appendix C)

$$\Gamma_\perp(x) = \frac{2}{x^2} \left(1 - e^{-x^2} [I_0 \left(\frac{R^2}{2r_c^2} \right) + I_1 \left(\frac{R^2}{2r_c^2} \right)] \right) \tag{4.15}$$

4.0.1. Density operator

In a next step, we write down equation (4.12) for both longitudinal (sapphire) and optical (diamond) phonons. For the latter, we get using equation (4.3)

$$\frac{d}{dt}\rho_t = -\frac{i}{\hbar}[H, \rho_t] - 2D_{\mathrm{CSL}}[\hat{q}_L[\hat{q}_L, \rho_t]] - 2D_{\mathrm{CSL}}[\hat{q}_R[\hat{q}_R, \rho_t]] \tag{4.16}$$

whereas for the former, we obtain

$$\frac{d}{dt}\rho_t = -\frac{i}{\hbar}[H, \rho_t] - D_{\mathrm{CSL}}[\hat{q}_L[\hat{q}_L, \rho_t]] - D_{\mathrm{CSL}}[\hat{q}_R[\hat{q}_R, \rho_t]] \tag{4.17}$$

We find that, for optical phonons, the diffusion rate D_{CSL} is amplified by a factor of 2, which simply reflects that we have two counter-oscillating atom lattices, each with collapse rate D_{CSL}. The rates D_{CSL} themselves are different for both setups, of course. We are thus able to give a value for the factor β introduced in equation (3.7): For optical phonons, we have $\beta = 2$, whereas for acoustic phonons we get $\beta = 1$. Let's appreciate for a moment what we achieved: We have a simple equation that gives the time evolution of the density operator, with an explicit form for D_{CSL}. To calculate $\Gamma(\vec{x}, \vec{y})$, we need to calculate this evolution in the position basis, i.e. we project on $\langle \vec{x}|.|\vec{y}\rangle$.

4.0.2. Position basis

What is the position basis here? Let us start with the most general case: For N particles, we have the basis $\{\left|x^L, x^R\right\rangle\}$, with $x^L = \{\vec{x}_i^L\}_{i=1}^N$ being the set of the positions of particles in the left diamond/sapphire, with $\vec{x}_i^L = (x_i^L, y_i^L, z_i^L)$. The index R refers to the right diamond/sapphire. We next separate this into COM motion (denoted by $\hat{\vec{X}}_i^L$) and relative

motion $\hat{\vec{r}}_i^L$, such that

$$\hat{\vec{x}}_i^L = \hat{\vec{X}}_i^L + \hat{\vec{r}}_i^L \tag{4.18}$$

In the setups presented here, the diamonds are at rest, such that the COM motion is zero. The relative displacement is just the position quadrature operator $\hat{x}_\alpha$ defined in equation (4.2). Using the notation from equation (4.3) for $\hat{x}_\alpha$ (remember, we just have single direction of excitation), we obtain

$$\hat{\vec{x}}_i^L = \hat{q}^L \tag{4.19}$$

and similarly for the label R. The basis we want is thus the tensor product of quadrature eigenstates $\{q^L, q^R\}$, i.e. we have

$$(\hat{q}^L \otimes \mathrm{Id}) \left|q^L, q^R\right\rangle = q^L \left|q^L, q^R\right\rangle \tag{4.20}$$

We can now make a simple approximation to estimate the CSL-induced decay of our superposition state

$$|\Psi\rangle = \frac{1}{\sqrt{2}} \left(|0_L, 1_R\rangle + |1_L, 0_R\rangle\right) \tag{4.21}$$

Recall that the relevant superposition is within each diamond and entanglement doesn't play a role for CSL effects. The superposition is between a given lattice *at rest* (with position ket $|0_L, 0_R\rangle$) and between the lattice vibrating if one or more phonons are excited, with corresponding ket $\left|q^L > 0, q^R > 0\right\rangle$. In simple terms, imagine that the atom lattice is a massive lump, at the center of a 1D grid. Then the superposition is between a lump at 0 (the lattice at rest) and between a lump at q (the lattice is displaced). We now project equation (4.17) onto the quadrature basis, yielding

$$\begin{aligned}\langle 0^L, 0^R| \frac{d}{dt}\hat{\rho}_t |q^L, q^R\rangle - \beta D_{\mathrm{CSL}} \langle 0^L, 0^R| [\hat{q}_L[\hat{q}_L, \rho_t]] |q^L, q^R\rangle - \\ - \beta D_{\mathrm{CSL}} \langle 0^L, 0^R| [\hat{q}_R[\hat{q}_R, \rho_t]] q^L, q^R\rangle\end{aligned} \tag{4.22}$$

We simplify the commutator and obtain

$$[\hat{q}_L[\hat{q}_L, \rho_t]] = \hat{q}_L^2 \hat{\rho} - 2\hat{q}_L \hat{\rho} \hat{q}_L + \hat{\rho} \hat{q}_L^2 \tag{4.23}$$

This, together with equation (4.20), yields

$$\langle 0^L, 0^R| \frac{d}{dt}\hat{\rho}_t |q^L, q^R\rangle = \beta D_{\mathrm{CSL}} q^L q^R \langle 0^L, 0^R| \frac{d}{dt}\hat{\rho}_0 |q^L, q^R\rangle \tag{4.24}$$

The solution of this equation is a simple exponential decay law. The density operator at time t in the position basis with initial operator $\hat{\rho}_0$ is hence

$$\langle 0^L, 0^R| \hat{\rho}_t |q^L, q^R\rangle = \langle 0^L, 0^R| \hat{\rho}_0 |q^L, q^R\rangle e^{-\beta D_{\mathrm{CSL}} q^L q^R t} \tag{4.25}$$

which is the exponential decay law from Section (3.3.2). We conclude that

$$\Gamma(\vec{x},\vec{y}) \to \Gamma(q^L, q^R) = -\beta D_{\mathrm{CSL}} q^L q^R t \tag{4.26}$$

What is the maximal decay rate that gives us the strongest possible bounds? Well, we certainly choose the largest possible displacement (q^L, q^R). To estimate this displacement, we calculate the variance of both quadrature operators. For a Fock state with n phonons $|n\rangle$, we find

$$\langle \hat{q}_i^2 \rangle = (2n+1) x_{\mathrm{ZPF}}^2 \tag{4.27}$$

giving an approximate maximal displacement of $q^L_{\mathrm{max}} = x_{\mathrm{ZPF}}\sqrt{2n+1}$. Inserting this maximal displacement for both quadratures into equation (4.25) gives a *maximal* decay rate

$$\Gamma(q^L, q^R) = -\beta D_{\mathrm{CSL}} x_{\mathrm{ZPF}}^2 (2n+1) t \tag{4.28}$$

For the setups presented here, we have one (delocalized) phonon, and hence get

$$\Gamma(q^L, q^R) = -\beta D_{\mathrm{CSL}} x_{\mathrm{ZPF}}^2 t \tag{4.29}$$

whereas the decay rate given in equation (4.28) would be valid for NOON states with phonon number $N \geq 2$. This is just the result from [25]. In Appendix D, we report the calculation for the Fock basis instead of the position basis, which might be useful for further research.

Chapter 5

Conclusion

The goal of this semester report was two-fold. We first gave an overview about quantum collapse models, and highlighted the two most important models in particular: The GRW model and the CSL model. We presented how collapse might be related to gravity, and explained the most important assumptions behind CSL theory.

Secondly, we explicitly calculated exlcusion zones for the "new" constants of nature in collapse theory, i.e. for the collapse rate λ and the localization length r_c, using two experimental setups. We compared our results against reference literature, in particular against the calculations of Belli et al. [25]. We re-derived the calculations there, and highlighted additional assumptions not mentioned in the reference paper. Most importantly, we presented a novel approach to calculate the phonon oscillator mass and used this updated value to obtain new parameter exclusion zones that differ by 15 orders of magnitude from the ones in the reference paper.

Confirming earlier literature, for the two setups presented, we do not obtain any new exclusion zones, meaning that possible regions where collapse theory does not contradict experimental evidence still exist. However, as of now, indirect tests of collapse theory provide much stronger bounds than direct tests, hence limiting the usefulness of the calculations presented here.

Appendix A

A

This Appendix is devoted to derive equation (4.12). To do so, we insert the linearized mass operator (4.11) into the CSL Liouvillian (2.23), yielding:

$$\frac{d}{dt}\rho_t = -\frac{i}{\hbar}[H,\rho_t] - \\ -\frac{\lambda}{2r_c^3\pi^{3/2}m_0^2}\sum_{\alpha,\alpha'}\int d\vec{r}_1\int d\vec{r}_2\mu_\alpha(\vec{r}_1)\mu_{\alpha'}(\vec{r}_2)I_{ij}(\vec{r}_1,\vec{r}_2)[(\hat{\vec{x}}_\alpha)_i,[(\hat{\vec{x}}_{\alpha'})_j,\rho_t]] \quad \text{(A.1)}$$

where the two indices α,α' are due to $\hat{M}$ appearing twice in the double commutator in (2.23), meaning that we have two different mass distributions, and $I_{i,j}$ is defined as

$$I_{ij}(\vec{r}_1,\vec{r}_2) = \frac{1}{r_c^2}\frac{1}{r_c^2}\int d\vec{x}e^{-[(\vec{x}-\vec{r}_1)^2+(\vec{x}-\vec{r}_2)^2]/2r_c^2}(\vec{x}-\vec{r}_1)_i(\vec{x}-\vec{r}_2)_j \quad \text{(A.2)}$$

Here, the dot product is written using Einstein summation notation with indices $i,j \in \{1,2,3\}$. We want to bring this into the form of equation (4.12), which we write down again below:

$$\frac{d}{dt}\rho_t = -\frac{i}{\hbar}[H,\rho_t] - \sum_\alpha D^\alpha_{\mathrm{CSL}}[(\hat{z}_\alpha)[(\hat{z}_\alpha),\rho_t]] \quad \text{(A.3)}$$

Defining a set of diffusion rates $D^{\alpha,\alpha'}_{\mathrm{CSL},ij}$ as below almost does the job:

$$-\frac{\lambda}{2r_c^3\pi^{3/2}m_0^2}\sum_{\alpha,\alpha'}\int d\vec{r}_1\int d\vec{r}_2\mu_\alpha(\vec{r}_1)\mu_{\alpha'}(\vec{r}_2)I_{ij}(\vec{r}_1,\vec{r}_2) = \\ = \sum_{\alpha,\alpha'}\sum_{i,j=x,y,z} D^{\alpha,\alpha'}_{\mathrm{CSL},ij} \quad \text{(A.4)}$$

except that we have to sort out the indices. We take a closer look at the left-hand side of the above equation: The mass distributions $\mu_\alpha,\mu_{\alpha'}$ refer to different spatial regions within the diamond or the sapphire, such that terms of the form $\int d\vec{r}_1\int d\vec{r}_2\mu_\alpha(\vec{r}_1),\mu_{\alpha'}(\vec{r}_2)$ vanish unless $\alpha=\alpha'$. We thus conclude

$$\sum_{\alpha,\alpha'} \to \sum_\alpha \Rightarrow D^{\alpha,\alpha'}_{\mathrm{CSL},ij} \to D^\alpha_{\mathrm{CSL},ij}$$

such that we finally have

$$D^{\alpha}_{\mathrm{CSL},ij} = \frac{\lambda}{2r_c^3\pi^{3/2}m_0^2}\sum_{\alpha}\int d\vec{r}_1\int d\vec{r}_2\mu_{\alpha}(\vec{r}_1)\mu_{\alpha'}(\vec{r}_2)I_{ij}(\vec{r}_1,\vec{r}_2) \tag{A.5}$$

This is, in general, difficult to evaluate. However, as outlined in Section (3.4) we have $\hat{\vec{x}}_{\alpha} = \hat{z}_{\alpha}$, such that the only nonzero integral I_{ij} in equation $(A.5)$ is I_{zz}. Its calculation is reported in [25], Appendix B. Here, we provide additional calculation to simplify the understanding. Using $\vec{u} = \vec{x} - \vec{r}_1$, $\vec{y} = \vec{r}_1 - \vec{r}_2$, (such that $\vec{x} - \vec{r}_2 = \vec{y} + \vec{u}$) we get

$$I_{33}(\vec{r}_1,\vec{r}_2) = I_{33}(\vec{y}) = \frac{1}{r_c^4}\int d\vec{u}e^{-[\vec{u}^2+(\vec{y}+\vec{u})^2]/2r_c^2}(\vec{u})_3(\vec{y}+\vec{u})_3 \tag{A.6}$$

Simplifying the exponent, this becomes

$$I_{33}(\vec{r}_1,\vec{r}_2) = \frac{e^{-\vec{y}^2/2r_c^2}}{r_c^4}\int\prod_{i=1,2,3}du_i e^{-[(u_i+u_iy_i)]2u_i/2r_c^2}(\vec{u})_3(\vec{y}+\vec{u})_3 \tag{A.7}$$

Every other step is outlined in Appendix B of paper [25], giving

$$I_{33}(\vec{r}_1,\vec{r}_2) = \frac{\pi^{3/2}}{2r_c}\exp\left\{-\frac{(\vec{r}_1-\vec{r}_2)^2}{4r_c^2}\right\}\left[r_c^3 - \frac{(\vec{r}_1-\vec{r}_2)_3^2}{4r_c^2}\right] \tag{A.8}$$

Inserting this into equation $(A.5)$ gives a closed-form expression for D_{CSL}. It is, however, more convenient to calculate D_{CSL} in momentum space, which is done in Appendix B.

B

Following [21], we write $\hat{M}$ as defined in equation (4.1) in momentum space

$$\hat{M}(\vec{x}) = \sum_{\alpha} \sum_{n \in A_\alpha} m_n e^{-[\vec{x}-(\vec{x}^{(0)}_{n,\alpha}+\hat{\vec{x}}_\alpha)]^2/2r_c^2} = \\ = \sum_{\alpha} \frac{r_c^3}{(2\pi)^{3/2}} \int d\vec{k} e^{-r_c^2 k^2/2} e^{i\vec{k}(\vec{x}-\hat{\vec{x}}_\alpha)} \mu_\alpha(\vec{k}) \quad \text{(B.1)}$$

In the following, we will simplify this expression using similar methods as for the position space derivation. First of all, note that we can rewrite the double commutator in (2.23) as

$$\mathcal{L}_{\text{CSL}}\hat{\rho} = -\frac{\lambda}{2r_c^3\pi^{3/2}m_0^2} \int d\vec{x} [\hat{M}(\vec{x}), [\hat{M}(\vec{x}), \hat{\rho}_t]] = \\ = -\frac{\lambda}{r_c^3\pi^{3/2}m_0^2} \int d\vec{x} \left(\frac{1}{2}\{\hat{M}^2(\vec{x}), \hat{\rho}\} - \hat{M}(\vec{x})\hat{\rho}\hat{M}(\vec{x}) \right) \quad \text{(B.2)}$$

Inserting $(B.1)$ into $(B.2)$ gives

$$\frac{\lambda}{r_c^3\pi^{3/2}m_0^2} \frac{r_c^6}{(2\pi)^3} \int d\vec{x} \sum_{\alpha,\alpha'} \int d\vec{k} \int d\vec{k'} e^{-\frac{r_c^2 k^2}{2r_c}} e^{-\frac{r_c^2 (k')^2}{2r_c}} \mu(\vec{k})_\alpha \mu(\vec{k'})_{\alpha'} e^{i\vec{x}(\vec{k}-\vec{k'})} * \\ * \left(e^{-i\vec{k}\hat{\vec{x}}_\alpha} \rho e^{-i\vec{k}\hat{\vec{x}}_{\alpha'}} - \frac{1}{2}\{e^{-i\vec{k}\hat{\vec{x}}_\alpha} e^{-i\vec{k'}\hat{\vec{x}}_{\alpha'}}, \rho\} \right) \quad \text{(B.3)}$$

which, using $\int d\vec{x} e^{i\vec{x}(\vec{k}-\vec{k'})} = \delta^{(3)}(\vec{k}-\vec{k'})(2\pi)^{3/2}$ and $[\hat{\vec{x}}_\alpha, \hat{\vec{x}}_{\alpha'}] = 0$, evaluates to

$$\frac{\lambda r_c^3}{m_0^2\pi^{3/2}} \sum_{\alpha} \int d\vec{k} e^{-r_c^2 k^2} |\mu(\vec{k})_\alpha|^2 (e^{-i\vec{k}\hat{\vec{x}}_\alpha} \rho e^{-i\vec{k}\hat{\vec{x}}_{\alpha'}} - \rho) \quad \text{(B.4)}$$

Expanding the left term in the bracket to second order and using $\hat{\vec{x}}_\alpha = \hat{z}_\alpha$ gives

$$e^{-ik_z z}\rho e^{ik_z z} = \left(\mathrm{Id} - ik_z z - \frac{k_z^2 z^2}{2} + ...\right)\rho\left(\mathrm{Id} + ik_z z - \frac{k_z^2 z^2}{2}\right) =$$
$$= \rho - ik_z z\rho + ik_z \rho z + \frac{k_z^2}{2}\left(z^2\rho - 2z\rho z + \rho z^2\right) =$$
$$= \rho - ik_z[z,\rho] + \frac{k_z^2}{2}[z,[z,\rho]] \quad \text{(B.5)}$$

Inserting this into $(B.3)$ gives

$$\mathcal{L}_{\mathrm{CSL}}\hat{\rho} = \frac{\lambda r_c^3}{m_0^2\pi^{3/2}}\sum_\alpha \int d\vec{k} e^{-r_c^2 k^2}|\mu(\vec{k})|^2 \frac{k_z^2}{2}[\hat{z},[\hat{z},\hat{\rho}]] \quad \text{(B.6)}$$

such that we find, identical to the expression for position space

$$\frac{d}{dt}\hat{\rho}_t = -\frac{i}{\hbar}[\hat{H},\hat{\rho}] - D^\alpha_{\mathrm{CSL}}\sum_\alpha [\hat{z}_\alpha,[\hat{z}_\alpha,\hat{\rho}]] \quad \text{(B.7)}$$

with

$$D^\alpha_{\mathrm{CSL}} = \frac{\lambda r_c^3}{2m_0^2\pi^{3/2}}\int d\vec{k} e^{-r_c^2 k^2}|\mu(\vec{k})|^2 k_z^2 \quad \text{(B.8)}$$

In the Appendix C, we will evaluate expression $(B.8)$.

Appendix C

C

By using Mathematica, we will calculate the following two expressions:

- First, the Fourier-transformed mass density $\mu(\vec{k})$

- Secondly, the integral in equation $(B.8)$ itself.

Recall that $\mu(\vec{r})$ is defined as (cf. Section (3.4)) as

$$\mu(\vec{r}) = \begin{cases} \frac{m}{V}, & \text{if } \vec{r} \in \mathcal{V} \\ 0, & \text{otherwise} \end{cases}$$

which yields

$$\begin{aligned} \mu(\vec{k}) = \int_{-\infty}^{\infty} d\vec{r}\mu(\vec{r})e^{-i\vec{k}\vec{r}} &= \frac{m}{V}\int_V dV e^{-i\vec{k}\vec{r}} \\ &= \frac{m}{\pi R^2 d}\int_0^R rdr\int_0^{2\pi} d\phi\int_{-d/2}^{d/2} e^{-ik_z z}e^{-i(k_x x+k_y y)}dz = \\ &= \frac{m}{\pi R^2 d}\int_0^R rdr\int_0^{2\pi} d\phi\int_{-d/2}^{d/2} e^{-ik_z z}e^{-ik_r r\cos\phi}dz = \\ &= \frac{m}{\pi R^2 d}\frac{4\pi R}{k_r k_z}\sin\frac{dk_z}{2}J_1(k_r R) = \frac{2m}{Rk_r}J_1(k_r R)\frac{\sin\frac{dk_z}{2}}{\frac{dk_z}{2}} \end{aligned} \quad \text{(C.1)}$$

where we solved the integral in polar coordinates, employed the Hankel transform, and used $k_r = \sqrt{k_x^2 + k_y^2}$. Defining now similarly $\sqrt{k_x^2 + k_y^2} = |k_\perp|$, we insert $(C.1)$ into $(B.8)$

and obtain

$$
\begin{aligned}
D_{\mathrm{CSL}} &= \frac{\lambda r_c^3}{2m_0^2\pi^{3/2}}\int d\vec{k}e^{-r_c^2k^2}|\mu(\vec{k})|^2k_z^2 = \\
&= \frac{\lambda r_c^3}{2m_0^2\pi^{3/2}}\frac{4m^2}{R^2}\int dk_z k_z^2\left(\frac{\sin\frac{dk_z}{2}}{\frac{dk_z}{2}}\right)^2 e^{-r_c^2k_z^2}\int dk_x dk_y\frac{|J_1(|k_\perp|R)|^2}{|k_\perp|^2}e^{-r_c^2|k_\perp|^2} = \\
&= \frac{\lambda r_c^3}{2m_0^2\pi^{3/2}}\frac{4m^2}{R^2}\frac{2\sqrt{\pi}}{d^2r_c}\left(1-e^{-d^2/4r_c^2}\right)\int dk_x dk_y\frac{|J_1(|k_\perp|R)|^2}{|k_\perp|^2}e^{-r_c^2|k_\perp|^2} = \\
&= \frac{\lambda r_c^3}{2m_0^2\pi^{3/2}}\frac{4m^2}{R^2}\frac{2\sqrt{\pi}}{d^2r_c}\left(1-e^{-d^2/4r_c^2}\right)2\pi\int_0^\infty drr\frac{|J_1(rR)|^2}{r^2}e^{-r_c^2r^2} = \\
&= \frac{\lambda r_c^3}{2m_0^2\pi^{3/2}}\frac{4m^2}{R^2}\frac{2\pi^{1/2}}{d^2r_c}\left(1-e^{-d^2/4r_c^2}\right)* \\
&\quad *2\pi\left(\frac{1}{2}-\frac{1}{2}e^{-R^2/2r_c^2}[I_0\left(\frac{R^2}{2r_c^2}\right)+I_1\left(\frac{R^2}{2r_c^2}\right)]\right) = \\
&= \lambda\left(1-e^{-R^2/2r_c^2}[I_0\left(\frac{R^2}{2r_c^2}\right)+I_1\left(\frac{R^2}{2r_c^2}\right)]\right)\left(1-e^{-d^2/4r_c^2}\right)\frac{4r_c^2m^2}{R^2m_0^2d^2} = \\
&= \lambda\frac{m^2}{d^2m_0^2}\Gamma_\perp\left(\frac{R}{\sqrt{2}r_c}\right)\left(1-e^{-d^2/4r_c^2}\right) \qquad \text{(C.2)}
\end{aligned}
$$

where

$$
\Gamma_\perp(x) = \frac{2}{x^2}\left(1-e^{-x^2}[I_0\left(\frac{R^2}{2r_c^2}\right)+I_1\left(\frac{R^2}{2r_c^2}\right)]\right) \qquad \text{(C.3)}
$$

Using $m = 12Nm_0$, this is equation (22) from [25]. We conclude that for a *cylindrical* geometry with *uniform* mass distribution, the diffusion rate D_{CSL} is given by

$$
D_{\mathrm{CSL}} = \lambda\frac{m^2}{d^2m_0^2}\Gamma_\perp\left(\frac{R}{\sqrt{2}r_c}\right)\left(1-e^{-d^2/4r_c^2}\right) \qquad \text{(C.4)}
$$

Appendix D

D

For completeness purposes, we include the Fock basis calculation here. We defined the initial density operator ρ_0 in Section (3.4) as

$$\rho_0 = \frac{1}{2}\begin{pmatrix} 0 & 0 & 0 & 0 \\ 0 & 1 & 1 & 0 \\ 0 & 1 & 1 & 0 \\ 0 & 0 & 0 & 0 \end{pmatrix}$$

This is in the Fock basis. We calculate the time evolution for the 16 elements in the following section. The simplified differential equation for ρ_t is given in equation ($D.7$), and the solution presented in a later section of this Appendix. More generelly speaking, we have basis elements $\{|n^R, n^L\rangle\}$, where $n^{(i)}, i \in \{L, R\}$ denotes the number of excitations in the the left or right diamond/sapphire. Depending on the experiment, $n \in \{0, 1\}$ (as above) or $\{0, k\}, k \leq N$. We want to project the density operator evolution equation (4.17) onto the above basis. To do so, we use equation (4.2), make a change of notation $\hat{a} \leftrightarrow \hat{b}$, and let the creation and annihilation operators act on the Fock states as

$$\hat{a}_L \otimes I_R \left|n^L, n^R\right\rangle = \sqrt{n}\left|(n-1)^L, n^R\right\rangle \tag{D.1}$$

$$\hat{a}^\dagger \otimes I_R \left|n^L, n^R\right\rangle = \sqrt{n+1}\left|(n+1)^L, n^R\right\rangle \tag{D.2}$$

Writing down the quadrature operator in terms of annihilation and creation operators, we obtain the following expression for the double commutator $[\hat{q}_J[\hat{q}_J, \rho_t]]$, where $J \in \{L, R\}$:

$$\begin{aligned}[\hat{q}_L[\hat{q}_L, \rho_t]] = \frac{x_{\text{ZPF}}^2}{2}\Big([\hat{a}, [\hat{a}, \hat{\rho}]] + [\hat{a}^\dagger, [\hat{a}, \hat{\rho}]][\hat{a}, [\hat{a}^\dagger, \hat{\rho}]] + [\hat{a}^\dagger, [\hat{a}^\dagger, \hat{\rho}]]\Big) = \\ = \frac{x_{\text{ZPF}}^2}{2}\Big(\hat{a}^2\hat{\rho} + \hat{\rho}\hat{a}^2 + (\hat{a}^\dagger)^2\hat{\rho} + \hat{\rho}(\hat{a}^\dagger)^2\Big) + \\ + \frac{x_{\text{ZPF}}^2}{2}\Big(-2\hat{a}\hat{\rho}\hat{a} - 2\hat{a}^\dagger\hat{\rho}\hat{a}^\dagger - 2\hat{a}\hat{\rho}\hat{a}^\dagger - 2\hat{a}^\dagger\hat{\rho}\hat{a}\Big) + \\ + \frac{x_{\text{ZPF}}^2}{2}\Big(\hat{a}^\dagger\hat{a}\hat{\rho} + \hat{\rho}\hat{a}\hat{a}^\dagger + \hat{a}\hat{a}^\dagger\hat{\rho} + \hat{\rho}\hat{a}^\dagger\hat{a}\Big)\end{aligned} \tag{D.3}$$

where we the first row above contains second-order terms that vanish for $N \leq 1$ and the second row yields the off-diagonal coupling terms. The third line is further simplified by

using $\hat{a}\hat{a}^\dagger = 1 + \hat{a}^\dagger\hat{a}$, and by defining $\hat{n} = \hat{a}^\dagger\hat{a}$. We get

$$\frac{x_{\mathrm{ZPF}}^2}{2}\left(\hat{a}^\dagger\hat{a}\hat{\rho} + \hat{\rho}\hat{a}\hat{a}^\dagger + \hat{a}\hat{a}^\dagger\hat{\rho} + \hat{\rho}\hat{a}^\dagger\hat{a}\right) = x_{\mathrm{ZPF}}^2\left(\hat{n}\hat{\rho} + \hat{\rho}\hat{n} + \hat{\rho}\right) \tag{D.4}$$

Doing now the projection, we obtain

$$\begin{aligned}
\langle n_i^R n_j^L|[\hat{q}_L[\hat{q}_L,\rho_t]]|n_k^R n_l^L\rangle = {} & \frac{x_{\mathrm{ZPF}}^2}{2}\sqrt{n_j^L+1}\sqrt{n_j^L+2}\langle n_i^R, n_j^L+2|\rho|n_k^R, n_l^L\rangle + \\
& + \frac{x_{\mathrm{ZPF}}^2}{2}\sqrt{n_l^L+1}\sqrt{n_l^L+2}\langle n_i^R, n_j^L|\rho|n_k^R, n_l^L+2\rangle + \\
& + \frac{x_{\mathrm{ZPF}}^2}{2}\sqrt{n_j^L-1}\sqrt{n_j^L}\langle n_i^R, n_j^L-2|\rho|n_k^R, n_l^L\rangle \\
& + \frac{x_{\mathrm{ZPF}}^2}{2}\sqrt{n_l^L-1}\sqrt{n_l^L}\langle n_i^R, n_j^L|\rho|n_k^R, n_l^L-2\rangle - \\
& - x_{\mathrm{ZPF}}^2\sqrt{n_j^L+1}\sqrt{n_l^L}\langle n_i^R, n_j^L+1|\rho|n_k^R, n_l^L-1\rangle - \\
& - x_{\mathrm{ZPF}}^2\sqrt{n_j^L}\sqrt{n_l^L+1}\langle n_i^R, n_j^L-1|\rho|n_k^R, n_l^L+1\rangle - \\
& - x_{\mathrm{ZPF}}^2\sqrt{n_j^L+1}\sqrt{n_l^L+1}\langle n_i^R, n_j^L+1|\rho|n_k^R, n_l^L+1\rangle - \\
& - x_{\mathrm{ZPF}}^2\sqrt{n_j^L}\sqrt{n_l^L}\langle n_i^R, n_j^L-1|\rho|n_k^R, n_l^L-1\rangle + \\
& + x_{\mathrm{ZPF}}^2(n_j^L+n_l^L+1)\langle n_i^R, n_j^L|\rho|n_k^R, n_l^L\rangle
\end{aligned} \tag{D.5}$$

An identical derivation holds for the commutator with $\hat{q}^R$ instead of $\hat{q}^L$, with replacements $n_j^L \Longleftrightarrow n_i^R$ and $n_l^L \Longleftrightarrow n_k^R$. Equation $(D.5)$ is valid for any $n_j, n_l, n_k, n_i \in N$. Here, we restrict ourselves to the set $n_j, n_l, n_k, n_i \in \{0,1\}$ such that we have a 4-dimensional basis and a total of 4x4 coupled equations $\rho_{ab}, a, b \in \{1,2,3,4\}$. We provide an example using the diagonal element ρ_{22}, i.e. we evaluate (4.17) for $n_j^L = n_l^L = 0, n_i^R = n_k^R = 1$ by inserting the simplified commutator from equation $(D.5)$. This yields

$$\begin{aligned}
\langle 0,1|\frac{d}{dt}\rho|0,1\rangle &= \langle 0,1|\left(-\frac{i}{\hbar}[H,\rho_t] - 2D_{\mathrm{CSL}}[\hat{q}_L[\hat{q}_L,\rho_t]] - 2D_{\mathrm{CSL}}[\hat{q}_R[\hat{q}_R,\rho_t]]\right)|0,1\rangle \\
&= -\frac{i}{\hbar}\langle 0,1|[H,\rho_t]|0,1\rangle - 2D_{\mathrm{CSL}} * \left(-x_{\mathrm{ZPF}}^2\langle 1,1|\rho|1,1\rangle + x_{\mathrm{ZPF}}^2\langle 0,1|\rho|0,1\rangle\right) - \\
&\quad - 2D_{\mathrm{CSL}} * \left(-x_{\mathrm{ZPF}}^2\langle 0,0|\rho|0,0\rangle + 3x_{\mathrm{ZPF}}^2\langle 0,1|\rho|0,1\rangle\right) = \\
&\quad = -\frac{i}{\hbar}\langle 0,1|[H,\rho_t]|0,1\rangle + 2D_{\mathrm{CSL}}x_{\mathrm{ZPF}}^2(\rho_{44} + \rho_{11} - 2\rho_{22})
\end{aligned} \tag{D.6}$$

which agrees with the expression given in equation (17) of [25]. In a similar manner, the remaining matrix elements ρ_{ab} with $a, b \in \{(0,0),(0,1),(1,0),(1,1)\}$ can be evaluated, yielding

$$\frac{d}{dt}\rho_{ab} = -\frac{i}{\hbar}\langle a|[H,\rho_t]|b\rangle - 2D_{\mathrm{CSL}}x_{\mathrm{ZPF}}^2(\Gamma[\rho])_{ab} \tag{D.7}$$

with

$$\Gamma[\rho] = \begin{pmatrix} 2\rho_{11}-\rho_{22}-\rho_{33} & 2\rho_{12}-\rho_{21}-\rho_{34} & 2\rho_{13}-\rho_{24}-\rho_{31} & 2\rho_{14}-\rho_{23}-\rho_{32} \\ 2\rho_{21}-\rho_{12}-\rho_{43} & 2\rho_{22}-\rho_{11}-\rho_{44} & 2\rho_{23}-\rho_{41}-\rho_{14} & 2\rho_{24}-\rho_{13}-\rho_{42} \\ 2\rho_{31}-\rho_{42}-\rho_{13} & 2\rho_{32}-\rho_{41}-\rho_{14} & 2\rho_{33}-\rho_{44}-\rho_{11} & 2\rho_{34}-\rho_{43}-\rho_{12} \\ 2\rho_{41}-\rho_{32}-\rho_{23} & 2\rho_{42}-\rho_{31}-\rho_{24} & 2\rho_{43}-\rho_{34}-\rho_{21} & 2\rho_{44}-\rho_{33}-\rho_{22} \end{pmatrix}$$

Solutions to the coupled equations

To solve equation $(D.7)$, we first do a Laplace-Transform of the 16 equations ρ_{ab}, solve, and then transform back to the time domain. Of the resulting solutions, 8 are trivial (i.e. $\rho_{ab} = 0$), 4 are imaginary and the remaining 4 are independent of ω. A complete Mathematica script, together with the solutions, is provided as well. The trivial solutions are $\rho_{12}, \rho_{21}, \rho_{13}, \rho_{31}, \rho_{24}, \rho_{42}, \rho_{34}, \rho_{43}$. The diagonal elements are real and given as

$$\rho_{11} = \rho_{44} = \frac{1}{4}\left(1 - e^{-2\Lambda t}\right) \tag{D.8}$$

$$\rho_{22} = \rho_{33} = \frac{1}{4}\left(1 + e^{-2\Lambda t}\right) \tag{D.9}$$

with $\Lambda = 4D_{\mathrm{CSL}}x_{\mathrm{ZPF}}^2$. It is obvious that $\rho_{ii} = \frac{1}{4}$ in the limit $t \to \infty$, as expected for a fully mixed state. For the imaginary solutions, we define $\Omega^2 = \Lambda^2 - 4\omega^2$ and obtain

$$\rho_{23} = \rho_{32} = e^{-\Lambda t}\frac{(\Lambda^2\cosh(\Omega t) - 4\omega^2)}{2\Omega^2} \tag{D.10}$$

$$\rho_{14} = \frac{\Lambda e^{-\Lambda t}}{2\Omega^2}\left(2i\omega\cosh(\Omega t) - 2i\omega + \Omega\sinh(\Omega t)\right) \tag{D.11}$$

$$\rho_{41} = \frac{\Lambda e^{-\Lambda t}}{2\Omega^2}\left(-2i\omega\cosh(\Omega t) + 2i\omega + \Omega\sinh(\Omega t)\right) \tag{D.12}$$

For the non-zero off-diagonal terms, we observe the following limits:

1. For $t \to \infty$: $\rho_{14} = \rho_{41} = \rho_{32} = \rho_{23} = 0$
2. For $t \ll 1$: Using $\cosh(\Omega t) \approx 1 + O(t^2)$ and $\sinh(\Omega t) \approx \Omega t + O(t^3)$, we find $\rho_{14} = \rho_{41} = \frac{\Lambda}{2}e^{-\Lambda t}(0+2) = \Lambda e^{-\Lambda t}$, as well as $\rho_{32} = \frac{e^{-\Lambda t}}{2}(\frac{\Omega^2}{\Omega^2}) = \frac{1}{2}e^{-\Lambda t}$

Figure $(D.1)$ illustrates the evolution of the off-diagonal for given values of Λ and ω. In the long-time limit, we have the fully mixed state

$$\rho_0 = \frac{1}{2}\begin{pmatrix} 0 & 0 & 0 & 0 \\ 0 & 1 & 1 & 0 \\ 0 & 1 & 1 & 0 \\ 0 & 0 & 0 & 0 \end{pmatrix} \xrightarrow{t\to\infty} \rho_t = \begin{pmatrix} 1 & 0 & 0 & 0 \\ 0 & 1 & 0 & 0 \\ 0 & 0 & 1 & 0 \\ 0 & 0 & 0 & 1 \end{pmatrix}$$

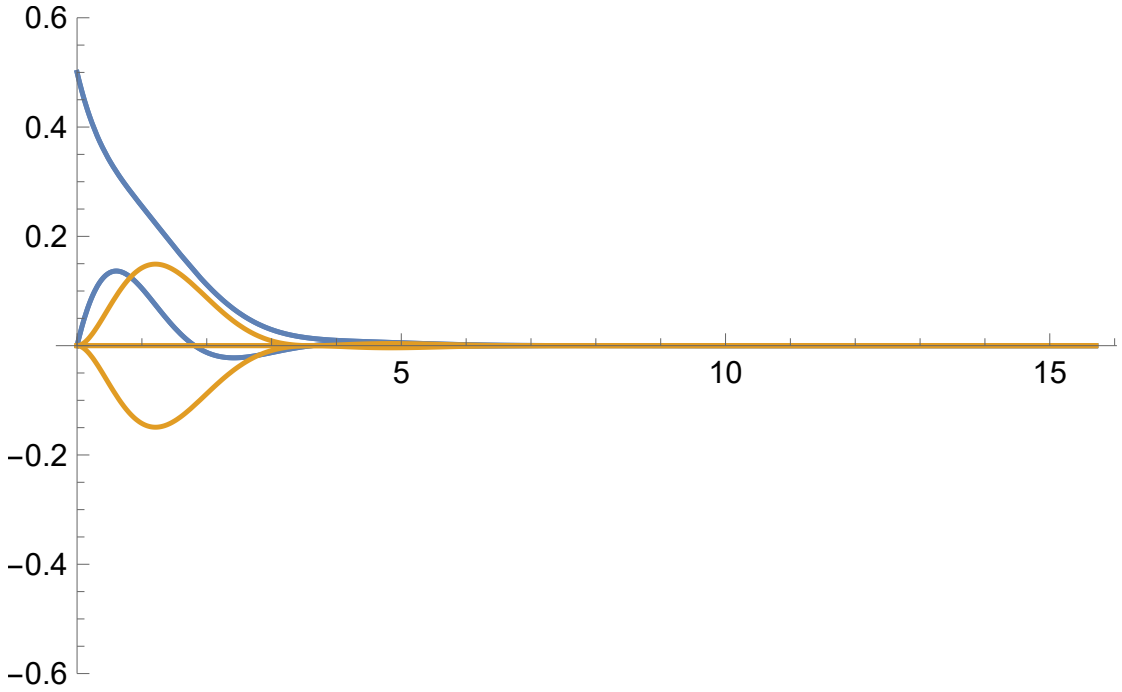

Figure D.1.: Plotted is a toy model of the time evolution of the imaginary and real parts of the non-zero off-diagonal terms ρ_{ij}. To illustrate the behavior of the various terms, we use values $\omega = 1\ s^{-1}$ and $\Lambda = 1$. The off-diagonals decay to zero, with ρ_{32} decaying from its inital value $\frac{1}{2}$ as expected.

Solving the coupled equations and neglecting H

In the previous section, we observed that the coherences ρ_{ij} decay to zero within a given timescale. This decay is both due to the coherent Hamiltonian evolution $\propto [\hat{H}, \hat{\rho}]$ and due to the CSL term $\propto \Lambda\Gamma[\rho]$. We now want to estimate the contribution of the CSL term to the total decay in the Fock basis. One possible approach to do so is to neglect the the coherent evolution and solve the resulting equation

$$\frac{d}{dt}\rho_{ab} = -2D_{\mathrm{CSL}} x^2_{\mathrm{ZPF}} (\Gamma[\rho])_{ab} \tag{D.13}$$

with $\Gamma[\rho]$ given as below equation (120). This system of coupled equations can be solved via a Laplace transform and yields 8 trivial solutions, as well as 8 real solutions. As expected, the evolution of the diagonal terms doesn't change since their time evolution is decoupled from the off-diagonal elements. The remaining 4 solutions, however, change and yield:

$$\rho_{14} = \rho_{41} = \frac{1}{4}\left(1 - e^{-2\Lambda t}\right) \tag{D.14}$$

$$\rho_{32} = \rho_{23} = \frac{1}{4}\left(1 + e^{-2\Lambda t}\right) \tag{D.15}$$

High-NOON

How does this analysis look like for higher-order NOON states? We provide a tentative calculation as an outlook, but couldn't complete the calculation due to time constraints. For a high-NOON state, we have the initial state $|\Psi\rangle = \frac{1}{\sqrt{2}}(|0,N\rangle + |N,0\rangle)$. The computational complexity to solve resulting system of equations increases quadratically, and the resulting system of coupled equations can only be solved numerically. We provide an example for the second-order NOON state given as

$$|\Phi_2\rangle = \frac{1}{\sqrt{2}}(|2,0\rangle + |0,2\rangle) \tag{D.16}$$

Restricting ourselves to a maximum number of two excitations per phonon mode, we obtain a $3^2 = 9$ dimensional basis set $\{|i,j\rangle\}$, $i,j \in 0,1,2$. As such, we have $9x9 = 81$ matrix elements ρ_{mn}, $m,n \in \{1,...,9\}$, where we follow the same naming convention as in the 4-dimensional case above. To estimate the order of magnitude of the CSL-induced decay, we have to determine

1. The initial density operator ρ_0 projected onto the above Fock basis, yielding a 9x9 matrix.
2. The CSL matrix $\Gamma[\rho]$, which is obtained by following the same procedure as in equation $(D.5)$. We will provide an example for this below.
3. The projection of the commutator $[\hat{H},\rho]$.

To demonstrate on how to obtain the CSL matrix $\Gamma[\rho]$, we calculate $\frac{d}{dt}\rho_{61} = \frac{d}{dt}\langle 12|\hat{\rho}_t|00\rangle$. We thus obtain

$$\langle 1,2|\frac{d}{dt}\rho|0,0\rangle \quad = \quad \langle 1,2|\left(-\frac{i}{\hbar}[H,\rho_t] - 2\eta[\hat{q}_L[\hat{q}_L,\rho_t]] - 2\eta[\hat{q}_R[\hat{q}_R,\rho_t]]\right)|0,0\rangle \tag{D.17}$$

We evaluate the CSL term by employing equation $(D.5)$, and use that by (our) definition $n_i^R = 1, n_j^L = 2, n_k^R = n_l^L = 0$. This yields (using a change of notation $D_{\mathrm{CSL}} = \eta$)

$$\begin{aligned}
&\langle 1,2|[\hat{q}_L[\hat{q}_L,\rho_t]]|0,0\rangle = \\
&\qquad = 0 + \frac{x_{\mathrm{ZPF}}^2}{2}\sqrt{2}\langle 1,2|\rho|0,2\rangle + \frac{x_{\mathrm{ZPF}}^2}{2}\sqrt{2}\langle 1,0|\rho|0,0\rangle + 0 - \\
&\quad - 0 - x_{\mathrm{ZPF}}^2\sqrt{2}\langle 1,1|\rho|0,1\rangle - 0 - 0 + x_{\mathrm{ZPF}}^2(2+0+1)\langle 1,2|\rho|0,0\rangle = \\
&\qquad = \frac{x_{\mathrm{ZPF}}^2}{\sqrt{2}}(\langle 1,2|\rho|0,2\rangle + \langle 1,0|\rho|0,0\rangle) - \\
&\quad - \sqrt{2}(x_{\mathrm{ZPF}}^2\langle 1,1|\rho|0,1\rangle + 3(\Delta z)^2\langle 1,2|\rho|0,0\rangle = \\
&\qquad = \frac{x_{\mathrm{ZPF}}^2}{\sqrt{2}}(\rho_{63} + \rho_{41}) - \sqrt{2}(\Delta z)^2\rho_{52} + 3x_{\mathrm{ZPF}}^2\rho_{61}
\end{aligned} \tag{D.18}$$

where we employed the naming convention in the last step.

Bibliography

1. Bassi, A. & Ghirardi, G. Dynamical reduction models. *Physics Reports* **379,** 257–426 (2003).
2. Schlosshauer, M. Decoherence, the measurement problem, and interpretations of quantum mechanics. *Rev. Mod. Phys.* **76,** 1267–1305 (4 2005).
3. Ghirardi, G. C., Rimini, A. & Weber, T. Unified dynamics for microscopic and macroscopic systems. *Phys. Rev. D* **34,** 470–491 (2 1986).
4. Ghirardi, G. C., Pearle, P. & Rimini, A. Markov processes in Hilbert space and continuous spontaneous localization of systems of identical particles. *Phys. Rev. A* **42,** 78–89 (1 1990).
5. Diósi, L. Models for universal reduction of macroscopic quantum fluctuations. *Phys. Rev. A* **40,** 1165–1174 (3 1989).
6. Carlesso, M., Paternostro, M., Ulbricht, H., Vinante, A. & Bassi, A. Non-interferometric test of the continuous spontaneous localization model based on rotational optomechanics. *New Journal of Physics* **20,** 083022 (2018).
7. Smirne, A. & Bassi, A. Dissipative Continuous Spontaneous Localization (CSL) model. *Scientific reports* **5,** 12518 (Aug. 2015).
8. Pearle, P. Combining stochastic dynamical state-vector reduction with spontaneous localization. *Phys. Rev. A* **39,** 2277–2289 (5 1989).
9. Pearle, P. Reduction of the state vector by a nonlinear Schrödinger equation. *Phys. Rev. D* **13,** 857–868 (4 1976).
10. Penrose, R. On gravity's role in quantum state reduction. *Gen. Rel. Grav.* **28,** 581–600 (1996).
11. Donadi, S. *et al.* Underground test of gravity-related wave function collapse. *Nature Physics* **17,** 74–78 (2020).
12. Gao, S. On Diósi-Penrose Criterion of Gravity-Induced Quantum Collapse. *International Journal of Theoretical Physics* **49,** 849–853 (2010).
13. Carlesso, M., Bassi, A., Falferi, P. & Vinante, A. Experimental bounds on collapse models from gravitational wave detectors. *Phys. Rev. D* **94,** 124036 (12 2016).
14. Carlesso, M., Ferialdi, L. & Bassi, A. Colored collapse models from the non-interferometric perspective. *The European Physical Journal D* **72** (2018).
15. Toroš, M., Gasbarri, G. & Bassi, A. Colored and dissipative continuous spontaneous localization model and bounds from matter-wave interferometry. *Physics Letters A* **381,** 3921–3927 (2017).

16. Eibenberger, S., Gerlich, S., Arndt, M., Mayor, M. & Tüxen, J. Matter–wave interference of particles selected from a molecular library with masses exceeding 10 000 amu. *Physical Chemistry Chemical Physics* **15,** 14696 (2013).

17. Lee, K. C. *et al.* Entangling Macroscopic Diamonds at Room Temperature. *Science* **334,** 1253–1256 (2011).

18. Fein, Y., Geyer, P., Zwick, P. & Arndt, M. Quantum Superposition of molecules beyond 25 kDA. *Nature Phys.* **15,** 1242–1245 (2019).

19. Donadi, S. *et al.* Novel CSL bounds from the noise-induced radiation emission from atoms. *The European Physical Journal C* **81** (2021).

20. Tilloy, A. & Stace, T. M. Neutron Star Heating Constraints on Wave-Function Collapse Models. *Physical Review Letters* **123** (2019).

21. Nimmrichter, S., Hornberger, K. & Hammerer, K. Optomechanical Sensing of Spontaneous Wave-Function Collapse. *Phys. Rev. Lett.* **113,** 020405 (2 2014).

22. Bahrami, M., Paternostro, M., Bassi, A. & Ulbricht, H. Proposal for a Noninterferometric Test of Collapse Models in Optomechanical Systems. *Physical Review Letters* **112** (2014).

23. Vinante, A., Mezzena, R., Falferi, P., Carlesso, M. & Bassi, A. Improved Noninterferometric Test of Collapse Models Using Ultracold Cantilevers. *Physical Review Letters* **119** (2017).

24. Vinante, A. *et al.* Narrowing the Parameter Space of Collapse Models with Ultracold Layered Force Sensors. *Physical Review Letters* **125** (2020).

25. Belli, S. *et al.* Entangling macroscopic diamonds at room temperature: Bounds on the continuous-spontaneous-localization parameters (2016).

26. Chu, Y. *et al.* Creation and control of multi-phonon Fock states in a bulk acoustic-wave resonator. *Nature* **563,** 666–670 (2018).

27. Chu, Y. *et al.* Quantum acoustics with superconducting qubits. *Science* **358,** 199–202 (2017).

28. Carlesso, M. *et al.* Present status and future challenges of non-interferometric tests of collapse models. *Nature Physics* **18,** 243–250 (2022).

29. Ferialdi, L. & Bassi, A. Continuous spontaneous localization reduction rate for rigid bodies. *Phys. Rev. A* **102,** 042213 (4 2020).